



THIS MANUSCRIPT HAS BEEN SUBMITTED TO THE JOURNAL OF GLACIOLOGY AND HAS NOT BEEN PEER-REVIEWED.

**Investigating the Dynamic History of a Promontory Ice Rise
using Radar Data**

Journal:	<i>Journal of Glaciology</i>
Manuscript ID	JOG-23-0111.R1
Manuscript Type:	Article
Date Submitted by the Author:	n/a
Complete List of Authors:	Ershadi, M. Reza; University of Tübingen Faculty of Science, Department of Geosciences Drews, Reinhard Drew; University of Tübingen Museum, Department of Geosciences Tison, Jean-Louis; ULB Université Libre de Bruxelles, Laboratoire de Glaciologie Martin, Carlos; British Antarctic Survey, Ice Dynamics and Paleoclimate Henry, Clara; University of Tübingen, Geosciences; Max Planck Institute for Meteorology Oraschewski, Falk; University of Tübingen Tsibulskaya, Veronica; Université Libre de Bruxelles, DGES Sun, Sainan; Northumbria University, Wauthy, Sarah; ULB Université Libre de Bruxelles, Laboratoire de Glaciologie Koch, Inka; University of Tübingen, Department of Geosciences Bons, Paul D.; Eberhard Karls, Geosciences Eisen, Olaf; Alfred Wegener Institute, Glaciology; University of Bremen, Geosciences Pattyn, Frank; Université Libre Bruxelles Faculte des Sciences, Laboratoire de Glaciologie
Keywords:	Ice rise, Radio-echo sounding, Anisotropic ice, Ice core, Antarctic glaciology

Abstract:

Ice rises hold valuable records revealing the ice dynamics and climatic history of Antarctic coastal areas from the Last Glacial Maximum to today. This history is often reconstructed from isochrone radar stratigraphy and simulations focusing on Raymond arch evolution beneath the divides. However, this relies on complex ice-flow models where many parameters are unconstrained by observations. Our study explores quad-polarimetric, phase-coherent radar data to enhance understanding near ice divides and domes, using Hammarrøygen Ice Rise (HIR) as a case study. Analysing a 5 km profile intersecting the dome, we derive vertical strain rates and ice-fabric properties. These align with ice core data near the summit, increasing confidence in tracing signatures from the dome to the flanks. The Raymond effect is evident, correlating with surface strain rates and radar stratigraphy. Stability is inferred over millennia for the saddle connecting HIR to the mainland, but dome ice-fabric appears relatively young compared to 2D model predictions. In a broader context, quad-polarimetric measurements provide valuable insights into ice-flow models, particularly for anisotropic rheology. Including quad-polarimetric data advances our ability to reconstruct past ice flow dynamics and climatic history in ice rises.

SCHOLARONE™
Manuscripts

Investigating the Dynamic History of a Promontory Ice Rise using Radar Data

M. Reza Ershadi¹, Reinhard Drews¹, Jean-Louis Tison², Carlos Martin³, A. Clara J. Henry^{1,4,5}, Falk M. Oraschewski¹, Veronica Tsibulskaya², Sainan Sun⁶, Sarah Wauthy², Inka Koch¹, Paul Bons¹, Olaf Eisen^{7,8}, and Frank Pattyn²

¹*Department of Geosciences University of Tübingen, Tübingen, Germany.*

²*Department of Geosciences, Environment, Society, Université libre de Bruxelles, Brussels, Belgium.*

³*British Antarctic Survey, Natural Environment Research Council, Cambridge, UK.*

⁴*Max Planck Institute for Meteorology, Hamburg, Germany.*

⁵*now at: Department of Mathematics, Stockholm University, Sweden*

⁶*Department of Geography and Environmental Sciences, Northumbria University, Newcastle upon Tyne, UK.*

⁷*Glaciology, Alfred Wegener Institute, Helmholtz Centre for Polar and Marine Research, Bremerhaven, Germany.*

⁸*Department of Geosciences, University of Bremen, Bremen, Germany.*

Correspondence: M. Reza Ershadi <mohammadreza.ershadi@uni-tuebingen.de>

ABSTRACT. Ice rises hold valuable records revealing the ice dynamics and climatic history of Antarctic coastal areas from the Last Glacial Maximum to today. This history is often reconstructed from isochrone radar stratigraphy and simulations focusing on Raymond arch evolution beneath the divides. However, this relies on complex ice-flow models where many parameters are unconstrained by observations. Our study explores quad-polarimetric, phase-coherent radar data to enhance understanding near ice divides and domes, using Hammarryggen Ice Rise (HIR) as a case study. Analysing a 5 km profile intersecting the dome, we derive vertical strain rates and ice-fabric properties.

26 **These align with ice core data near the summit, increasing confidence in**
27 **tracing signatures from the dome to the flanks. The Raymond effect is evident,**
28 **correlating with surface strain rates and radar stratigraphy. Stability is inferred**
29 **over millennia for the saddle connecting HIR to the mainland, but dome ice-**
30 **fabric appears relatively young compared to 2D model predictions. In a broader**
31 **context, quad-polarimetric measurements provide valuable insights into ice-**
32 **flow models, particularly for anisotropic rheology. Including quad-polarimetric**
33 **data advances our ability to reconstruct past ice flow dynamics and climatic**
34 **history in ice rises.**

35 1. INTRODUCTION

36 Ice rises are grounded, locally elevated, ice features surrounded by ice streams or ice shelves. They form
37 over regions with shallower bathymetry, enabling the accumulated ice to stay grounded in these areas.
38 This then results in a locally different flow regime (Matsuoka and others, 2015). Promontory ice rises, such
39 as Hammarryggen Ice Rise (HIR) (Fig. 1), are connected to the main ice sheet via a saddle in the surface
40 topography. They may form triple junctions near their domes (blue lines in Fig. 1), from which three
41 ridges extend into the ice-rise flanks. Ice rises have two main characteristics that make them of particular
42 interest: Firstly, they decelerate ice flux from the main ice sheet towards the ocean and consequently
43 delay grounding-line retreat (Favier and others, 2012, 2014; Favier and Pattyn, 2015; Schannwell and
44 others, 2019; Henry and others, 2022). Secondly, they are an archive for the local atmospheric and
45 ice-dynamic history. The latter is accessible through the englacial stratigraphy, which includes Raymond
46 arches—anticlines in the ice stratigraphy that evolve once a local ice dome or ice divide has formed
47 (Raymond, 1983). The presence or absence of Raymond arches provides insight into the ice-rise history,
48 especially the temporal stability of the configuration, and can be used as a tie-point of the ice thickness to
49 constrain continental ice-flow models. Such tie-points are important, as other constraints, such as exposure
50 dating of rock outcrops (Davies and others, 2012), are unavailable for most of the Antarctic perimeter.

51
52 Much progress in previous studies has guided the interpretation of observed Raymond stacks (i.e.,
53 individual Raymond arches and their evolution with depth) in the context of the ice-dynamic history

54 of a respective catchment (Matsuoka and others, 2015). Clear signatures of transience are Raymond
55 stacks that do not align with contemporary ice divides (Nereson and Waddington, 2002), such as at Siple
56 Dome (Nereson and others, 1998). Fully evolved Raymond stacks that align with the contemporary ice
57 divide location are at the other end of the spectrum and indicate stability (e.g., Derwael Ice Rise; Drews
58 and others (2015)). Cases between these two end members (Goel and others, 2020) are more difficult
59 to interpret and require advanced model-data comparison, including thermomechanically-coupled full
60 Stokes models with anisotropic rheology (Martín and others, 2009a,b; Martín and Gudmundsson, 2012)
61 and a dynamically evolving grounding line (Schannwell and others, 2019, 2020; Henry and others, 2022).

62

63 A drawback of the model-guided interpretation of observed Raymond stacks is that many unconstrained
64 factors influence the arch amplitude. One of them being the ice anisotropy (Martín and Gudmundsson,
65 2012; Drews and others, 2015) for which so far virtually no observations away from ice cores were
66 available. This is the main problem that we address in this paper using polarimetric radar as a main
67 tool. Arch amplitude is influenced by multiple interrelated factors that affect the development of ice
68 fabric. Firstly, the degree of non-linearity in Glen's flow law exponent significantly impacts arch size; a
69 higher non-linearity typically results in larger arch amplitudes (Gillet-Chaulet and others, 2011; Martín
70 and others, 2009a,b; Drews and others, 2015; Bons and others, 2018). In contrast, the along-ridge flow
71 component generally produces smaller arches (Martín and others, 2009a,b). Similarly, variations in bed
72 topography can lead to smaller arches when the bed is uneven (Kingslake and others, 2014), while basal
73 sliding also contributes to reduced arch sizes (Petit and others, 2003). Additionally, localized factors
74 such as surface mass balance and erosion at the crest can increase arch amplitudes (Drews and others,
75 2015; Conway and Wilbour, 1999). The historical thinning or thickening of the ice further translates to
76 changes in arch sizes relative to their current geometry (Martín and others, 2006; Goel and others, 2018).

77

78 Ice-core analysis, in combination with shallow and deep radar, can constrain the three-dimensional
79 ice geometry (Hindmarsh and others, 2011) and the surface accumulation history (Philippe and others,
80 2016; Goel and others, 2017; Cavitte and others, 2022). Strain measurements such as the coffee-can
81 method (Hamilton and Whillans, 2000) and repeat surveys with phase-coherent radar can provide
82 additional constraints on the vertical strain rates (Kingslake and others, 2014). However, other factors,
83 such as ice anisotropy, remain unconstrained, resulting in ambiguous matching of observed Raymond arch

84 stacks with ice-flow models (Drews and others, 2015). Consequently, so far, ice rises and their inferred
85 dynamic history play a minor role in constraining larger-scale ice flow models (Bentley and others, 2014).

86

87 Phase coherent radar polarimetry using a ground-based phase-sensitive Radio Echo Sounder (pRES)
88 (Brennan and others, 2014) has seen much development in terms of inferring ice-fabric types for
89 various flow regimes using the polarimetric coherence phase as a metric to extract information
90 from the birefringent radar backscatter (Dall, 2010; Jordan and others, 2019, 2020; Ershadi and
91 others, 2022; Rathmann and others, 2022; Zeising and others, 2023). Anisotropic ice-flow models
92 of steady-state ice rises, as detailed in studies by Martín and others (2009a,b); Martín and
93 Gudmundsson (2012), predict significant gradients in ice-fabric types on either side of an ice divide.
94 This prediction, highlighting the impact of anisotropic rheology on ice dynamics. However, thus far,
95 it has not been directly compared with observations, a gap that warrants attention in the field.

96

97 Here, we investigate to what extent ice-fabric properties can be derived from quad-polarimetric radar data
98 near a triple junction of HIR in Dronning Maud Land, East Antarctica. We validate the inferred ice-fabric
99 types with ice-core data near the summit and provide additional context in terms of variability in vertical
100 strain rates and corresponding signatures in the radar stratigraphy.

101 2. STUDY AREA & DATA

102 HIR is a promontory ice rise located in eastern Dronning Maud Land (Fig. 1). It has a discernible dome at
103 367 meter above sea level (masl) (Howat and others, 2022) that is co-located with a triple junction from
104 which three ridge divides extend into the ice-rise flanks. The ice thickness at the dome is approximately
105 550 m (Fig. A1). The average accumulation rate and mean ice thickness within the 5 km pRES profile
106 are reported as 0.4 m/a (Cavitte and others, 2022) and 550 m, respectively. The ratio of both values
107 (thickness/accumulation) provides a characteristic time scale (t_D), which is a reference of the time it takes
108 for a change to advert through the system (Martín and others, 2009a). For HIR, t_D is approximately 1400
109 years. In this study we use three different dataset collected at HIR.

110 **Phase coherent radar data:** In 2019, 15 static, quad-polarimetric measurements were taken along a 5
111 km profile crossing the triple junction HIR in northwest-to-southeast direction (Fig. 1b - red line). At each
112 site, we infer the magnitude and the orientation of ice fabric with depth (sect. 3.1). One static measurement
113 (site name p0) was taken at a few tens of metres distance from the ice core, which validates our inference

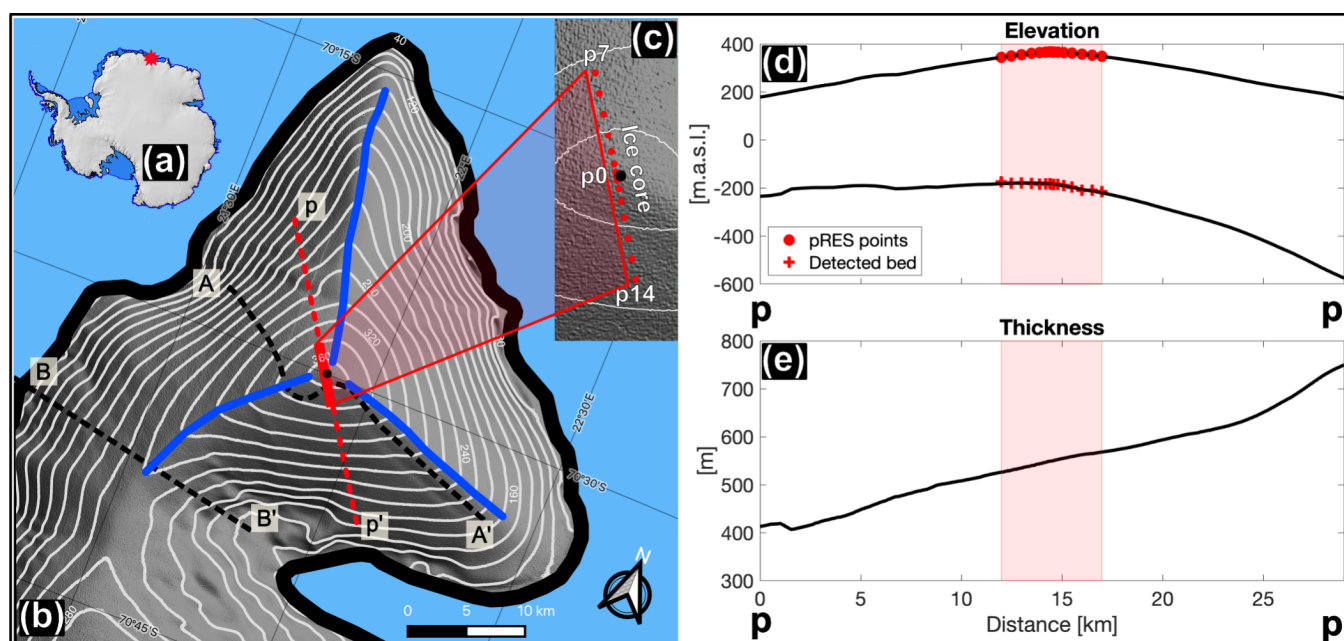


Figure 1: (a) The location of study area in Antarctica. (b) Hammarrýggen ice rise, the white contour lines and satellite background represents the surface elevation derived from the REMA dataset (Howat and others, 2022). Two black dashed lines represent the UWB flight lines. The blue lines denote the approximate position of the ridges. The black dot represents the location of the ice core and, the red line indicates the pRES profile. (c) The red shading corresponds to the location of the pRES profile. pRES measurement points depicted as red dots in the inset. (d) and (e) A cross-sectional view along the extended pp' profile, illustrating surface elevation (Howat and others, 2022), bed elevation and ice thickness (Morlighem, 2022).

114 with values derived from ice-core data (sect. 3.2). In 2020, all static sites were revisited to determine the
 115 yearly-averaged vertical strain rates (sect. 3.3).

116 **Airborne radar data:** The airborne radar data were collected in December 2018 and January 2019 as
 117 part of CHIRP (Channel and Ice Rise Project; Jansen and others, in: Fromm and others (2019)) using
 118 the ultra-wideband radar system (UWB) of the Alfred-Wegener-Institut Helmholtz-Zentrum für Polar- und
 119 Meeresforschung (2016) with a frequency range of 150-520 MHz. The system was deployed to survey the
 120 area providing ice thickness and internal ice stratigraphy data (sect. 3.4) at multiple cross sections roughly
 121 oriented along the East-West direction (Fig. 1b - black dashed lines).

122 **Ice core fabric data:** During the 2018-2019 austral summer field season, a 263 m long ice core was
 123 drilled at the summit of HIR (70.49960°S, 21.88019°E) (Fig. 1b - black dot). The ice core provided the
 124 age-depth relationship used to date near-surface radar stratigraphy imaged with a different ground-based
 125 radar in order to extrapolate the surface mass balance spatially (Cavitte and others, 2022). The ice core

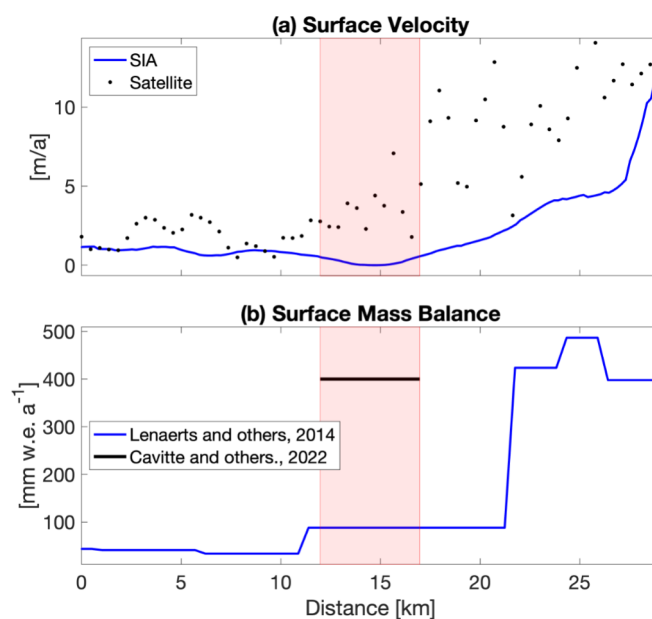


Figure 2: A cross-sectional view along the extended pp' profile (Fig. 1), illustrating (a) surface velocity (Shallow-ice approximation and Rignot and others (2017)), and (b) surface mass balance (Lenaerts and others, 2014; Cavitte and others, 2022). The red shading corresponds to the location of the pRES profile.

126 was also analysed to investigate ice crystal fabric. In this study we will only use the ice core fabric data to
 127 verify inferences drawn from 15 quad-polarimetric radar observations.

128 This publication marks the first release of all the data presented here, with the exception of the AA'
 129 UWB profile (illustrated by the black dashed lines in Fig. 1b), which was previously published by Koch
 130 and others (2023a). Additionally, an approximation of surface velocities and corresponding horizontal strain
 131 rates based on the shallow ice approximation (SIA) (sect. 3.5) is provided.

132 3. METHODS

133 3.1. Ice-fabric derived from static, phase-coherent radar

134 Propagation of radio waves through ice is polarization dependend because ice is mechanically and
 135 dielectrically anisotropic (Hargreaves, 1977, 1978; Fujita and others, 2006). More specifically, radio wave
 136 speed depends on the orientation of the ice crystals relative to the radio-wave polarization which leads
 137 to variability in backscattered power (through birefringence and anisotropic reflections) as a function of
 138 antenna orientation at the surface. The degree and type of anisotropy in ice, in short the ice-fabric type,
 139 is often described using three eigenvectors ($\vec{v}_1, \vec{v}_2, \vec{v}_3$) and eigenvalues ($\lambda_1, \lambda_2, \lambda_3$ with $\lambda_1 < \lambda_2 < \lambda_3$ and
 140 $\lambda_1 + \lambda_2 + \lambda_3 = 1$) which correspond to an ellipsoid best describing the bulk orientation of individual crystal

141 c-axis at a given depth. The directions are locally defined, but can be georeferenced using the antenna
142 orientation at the surface. Inferring the anisotropic ice properties from polarimetric radar data has been the
143 subject of many previous studies (Dall, 2010; Jordan and others, 2019, 2020; Ershadi and others, 2022;
144 Zeising and others, 2023) and some consensus has emerged that the polarization dependence can be fully
145 captured using a quad-polarimetric setup in which four antennas are oriented perpendicularly to each other.
146 Following the notation from the satellite remote sensing literature, the two orthogonal polarisations are
147 referred to as horizontal (H) and vertical (V), although they are both situated in the horizontal plane. Each
148 quad-polarimetric measurement consists of four individual measurements with co-polarised (HH, VV) and
149 cross-polarized (HV, VH) orientations. The data can be synthesised to mimic a full azimuthal orientation of
150 the antennas, and variations in backscatter power are displayed correspondingly (Young and others, 2020;
151 Ershadi and others, 2022, 2024).

152 Here, the quad-polarimetric data (Pattyn and others, 2023) at each site were collected with a fixed
153 antenna distance (5 m between centres), and the absolute, georeferenced orientation of the baseline
154 connecting the two antennas is determined with a compass with approximately 15° uncertainty. We
155 determine the horizontal ice fabric anisotropy ($\Delta\lambda_H = \lambda_2 - \lambda_1$) and its georeferenced orientation as
156 the direction of the strongest horizontal eigenvector (\vec{v}_2) using a polarimetric forward model (Fujita
157 and others, 2006) and an inversion outlined in Ershadi and others (2022). This method employs
158 HH and HV power anomaly data and the HHVV coherence phase, defined as the argument of the
159 complex polarimetric coherence and its scaled phase derivative, which estimates the depth variability of
160 $\Delta\lambda_H$ and \vec{v}_2 assuming that one (in this case \vec{v}_3) of the eigenvectors is pointing vertically. Additionally,
161 the method allows for the estimation of all three eigenvalues assuming that ice is isotropic at the
162 surface. This enables the reconstruction of the vertical anisotropy ($\Delta\lambda_V = \lambda_3 - \lambda_2$) in a top-to-
163 bottom approach. In this case a weak $\Delta\lambda_H$ would be reflected in a smoothly varying coherence phase.
164 A strong $\Delta\lambda_H$, on the other hand, would result in multiple nodes where the coherence phase is
165 wrapped at the 2π boundaries. For HIR specifically, we limit our analysis to a magnitude of coherence
166 of 0.4 following recommendations from Jordan and others (2019). This covers approximately the
167 upper 400 m, corresponding to approximately 70% of the total ice thickness near the dome (Fig. A1).

168

169 To categorize the various observed ice fabric types and their development at different depths, we employ
170 a classification method that uses the logarithmic ratios of the eigenvalues. This approach effectively

171 distinguishes between cluster-type (point maximum) and girdle-type fabrics, as outlined by Woodcock
172 (1977). The key parameters in this scheme are $K = \frac{\ln(\lambda_3/\lambda_2)}{\ln(\lambda_2/\lambda_1)}$ and $C = \ln(\lambda_3/\lambda_1)$, where K serves to identify
173 whether the fabric is a uniaxial girdle or cluster, and C measures the intensity of the identified ice fabric
174 type. K and C are later referred to as “Woodcock parameters”. The evolution of fabric types in relation to
175 flow regimes is well documented by Llorens and others (2022) providing comprehensive models and visual
176 representations that elucidate the relationship between ice deformation and the resultant fabric patterns.

177 3.2. Ice-fabric from ice-core data

178 The ice core was cut in 0.5 m sections on site, then packed, transported to and stored at the
179 Laboratoire de Glaciologie (Université libre de Bruxelles (ULB), Belgium) respecting the cold chain
180 (temperature below -25°C) at all times. Dating and interpretation of a series of environmental
181 and climatic proxies for the upper 120 metres of the core are beyond the scope of this paper
182 and are in Wauthy and others (2023) presented separately. Here we will focus on the ice-
183 fabric properties of the entire ice core, more specifically the eigenvalues of the eigenvectors,
184 characterizing the ice-fabric anisotropy that we aim to reconstruct from the pRES measurements.
185

186 To determine the eigenvalues of the ice fabric from the ice core, 114 regularly spaced 8 cm high and 500
187 μm thick vertical thin sections of ice were produced following the standard procedure of Langway (1958).
188 The thickness of the ice core sections, typically between 500 μm and 600 μm , ensures that there is no
189 superposition of crystals, allowing for accurate 3D fabric analysis. The Automatic Fabric Analyzer effectively
190 measures the orientation of individual pixels and uses image analysis to determine grain boundaries and
191 calculate the mean orientation within each grain, providing robust data for deriving eigenvectors. Crystal
192 (optic) c-axes orientations were measured using the G-50 Automated Ice Fabric Analyzer (Russell-Head
193 Instruments, e.g., Wilson and others (2003)). Eigenvectors and eigenvalues were calculated using the FAME
194 software (Hammes and Peternell, 2016). The same software was used to determine grain boundaries, to plot
195 c-axis orientation density distributions in a lower hemisphere, equal-area or Schmidt diagram. Schmidt
196 diagrams are a common representation in geology providing equi-areal 2D projections of the ice crystal’s
197 c-axes intersection with a lower hemisphere into the equatorial plane, chosen in the plane of the vertical
198 thin sections in this study. Density diagrams are constructed by counting the number of c-axes falling in a
199 reference counting circle displaced on a regular grid across the Schmidt diagram.

200 **3.3. Vertical strain rate**

201 The sites used for the polarimetric surveys (sect. 3.1) were marked with bamboo stakes and revisited one year
202 later. The phase-coherent repeat measurements enable tracking of the submergence of internal reflections
203 relative to the bed (Kingslake and others, 2014). This allows us to infer yearly averaged vertical strain
204 rates, a method which is commonly applied to ice shelves in order to isolate the basal melt rate signal from
205 observed thickness change (e.g., Nicholls and others (2015); Sun and others (2019)). For HIR specifically,
206 we calculated depth-averaged values of vertical strain rate for ice thickness intervals over tens of metres in
207 order to highlight signatures of the Raymond effect.

208 **3.4. Airborne radar data**

209 The UWB radar is an improved version of the Multichannel Coherent Radar Depth Sounder (MCoRDS
210 5) developed at the University of Kansas, Center for Remote Sensing and Integrated Systems (Rodriguez-
211 Morales and others, 2014; CReSIS, 2021), operated on AWT's Polar6 BT-67 aircraft (Wesche and others,
212 2016). The radar system consists of an eight-element antenna array polarised in HH, which serves as a
213 transmitter and receiver unit for radar signals. Data acquisition and processing methods are detailed in
214 Koch and others (2023a) and are similar to those described by Franke and others (2021) and Franke and
215 others (2022). During CHIRP, the radar transmitted three-stage linear modulated chirp signals (1 μ s low-
216 gain, 1 μ s high-gain and 3 μ s high-gain to sound the upper, middle and deeper part of the ice column in
217 high quality) in a frequency range of 150-520 MHz and at an acquisition height of \sim 360 m above the ice
218 surface. Radar data processing was conducted with the CReSIS Toolbox (CReSIS, 2021) and comprises pulse
219 compression, synthetic aperture radar (SAR) processing with a wide angular range, and array processing
220 (Rodriguez-Morales and others, 2014; Hale and others, 2016; Franke and others, 2022). The processed radar
221 data have a range resolution of \sim 0.35 m and an along-track trace spacing of approximately 6 m. Here, we
222 use selected sections of the airborne radar data to analyse signatures of the Raymond arches beneath the
223 dome and the landward-oriented ice divide (Fig. 1).

224 **3.5. Shallow Ice Approximation: Surface Velocities and Strain Rates**

225 Surface velocities at HIR are too low to be reliably measured up by remote sensing data. Therefore, we
226 use the shallow-ice approximation (SIA; Hutter (1983); Greve and Blatter (2009)) as a rough estimate of
227 the surface velocity and maximum horizontal strain rate ($\dot{\epsilon}_{max}$), whilst being aware that a higher-order
228 ice flow model would be more accurate in the region. We use the calculated surface flow direction and

229 the maximum strain rate direction, $\hat{\epsilon}_{max}$, to compare with the estimated strongest horizontal anisotropy
230 eigenvector, \vec{v}_2 . The map of HIR with the estimated magnitude and orientation of the surface velocity and
231 maximum horizontal strain rate is shown in Appendix D.

232 Our calculation of velocities using SIA is not without uncertainty. Although bed elevation errors in
233 BedMachine data are relatively low at Hammarryggen Ice Rise, there are some error estimates of up to
234 ~ 100 m on the southern side of the ice rise away from the radar profile (Morlighem and others, 2020).
235 Furthermore, we have made the assumption that ice is isothermal, but given that we are most interested in
236 comparing strain rate directions with the observational anisotropy data rather than strain rate magnitudes,
237 errors due to this assumption are likely to be small.

238 4. RESULTS

239 4.1. Inference of ice-fabric parameters from pRES measurements

240 We use the pRES measurement site closest to the ice-core site (marked p0 in Fig. 1) to illustrate results
241 from the quad-polarimetric analysis. The observations from the quad-polarimetric measurements are
242 displayed using multiple metrics. The HH power anomaly (Fig. 3a) represents the backscatter dependence
243 as a function of antenna orientation and is indicative of anisotropic reflections, e.g., due to vertical
244 variability in ice-fabric strength. The HHVV coherence phase (Fig. 3b) shows the phase correlation
245 between the HH and VV directions. Stronger vertical gradients correspond to a stronger $\Delta\lambda_H$. The HV
246 power anomaly (Fig. 3c) is an analogue to the HH power anomaly but for the depolarization component
247 and is a proxy for the ice-fabric orientation (marked with green dots). The scaled phase derivative
248 (Fig. 3d) of the ice-fabric orientation for a given depth interval (marked with green dots) is defined as
249 $\Delta\lambda_H$. Fig. 3e to f show the same metrics based on a radio-wave propagation model (Fujita and others,
250 2006) and ice-fabric parameters resulting from a non-linear optimization method (Ershadi and others, 2022).

251

252 The characteristic signatures (e.g., nodes, location of maxima, etc.) in the observations (Fig. 3a-d) are
253 well reproduced by the optimised forward model output (Fig. 3e-h) demonstrating that the inferred ice-
254 fabric eigenvalues and their changes with depth are adequately captured by the inversion. The gradient in
255 the polarimetric phase coherence indicates a gradual strengthening of $\Delta\lambda_H$ with depth, and the minima in
256 the HV power anomaly suggest that the ice-fabric orientation changes are small with depth. An exception
257 occurs in the depth interval between 150 and 200 m, where a cross-polarization extinction node suggests

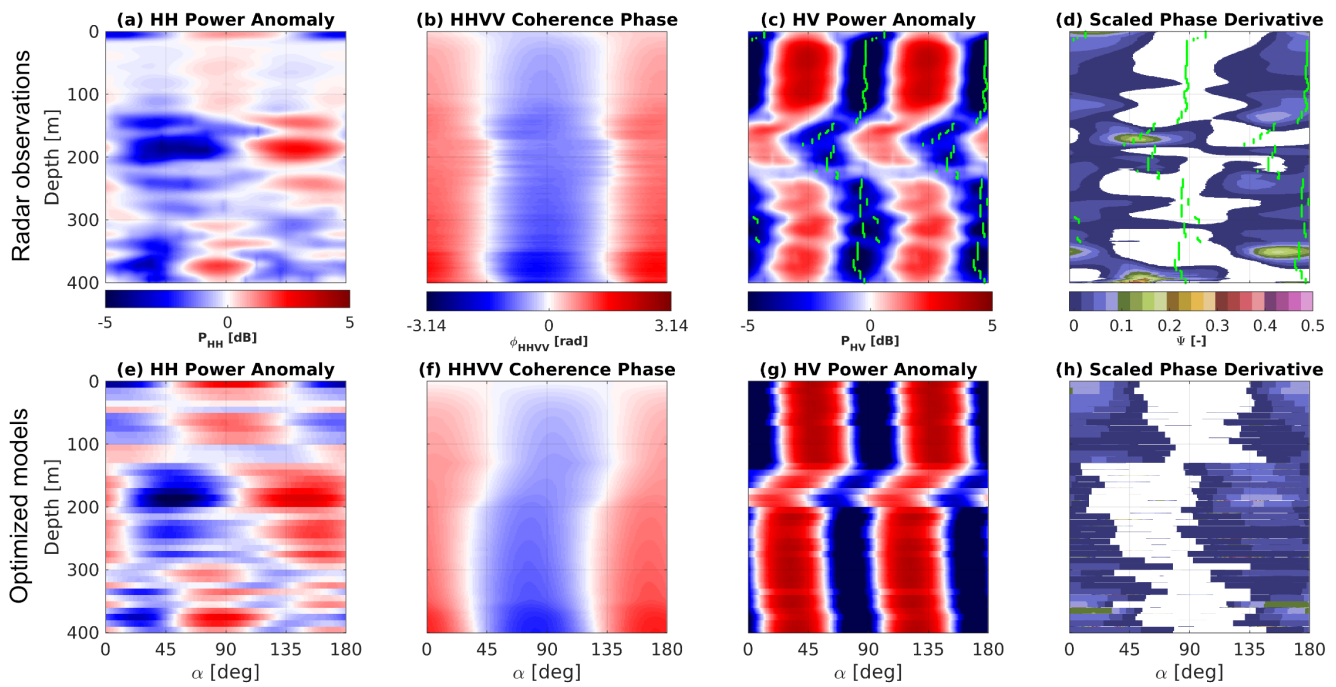


Figure 3: Results for the p0 radar site: (a) to (d) pRES observations, with green dots in (c) and (d) marking the minima in PHV. (e) to (h) Optimised model output capturing the principal patterns of the observations.

258 a rotation of the \vec{v}_2 eigenvector of several degrees (see Fig. 3c,g). We first substantiate the inferred ice-
 259 fabric parameters from the radar polarimetry by comparing them to ice-core measurements in the following
 260 section, and then continue by tracing the ice-fabric parameters away from the ice core into the ice-rise
 261 flanks.

262 4.2. Ice core validation

263 The fabric data measured from ice core samples show an increase with depth of λ_3 and a decrease of
 264 both λ_1 and λ_2 (Fig. 4). The measured $\Delta\lambda_H$ indicates a weak horizontal anisotropy within the ice
 265 column and remains almost constant with depth. In contrast the measured $\Delta\lambda_V$ increases with depth.
 266 This behaviour of eigenvalues results in Woodcock parameters $K > 1$ and $C < 2$ which categorize
 267 the fabric type into the weak uniaxial cluster. This behaviour is also visible in the density Schmidt
 268 diagrams (increasing areal concentration of crystals c-axes from white to red) shown in Fig. 4c for samples
 269 below 150 m where the distribution of the crystals slowly (low values on the density scale) evolves from a
 270 more random distribution in the top of the ice core towards a single maximum closely centred on the vertical.

271

272 The estimated eigenvalues from the quad-polarimetric radar measurement at site p0 are compared
273 with the measured ice-core eigenvalues (Fig. 4). The estimated eigenvalues and anisotropy in both
274 the horizontal and vertical directions exhibit the same behavior as the measured ones. However
275 the estimated λ_1 and λ_2 (Fig. 4a) are about 0.07 and 0.03 larger than the measured values,
276 respectively, and consequently, the estimated λ_3 is systematically smaller than the measured value.
277 Both estimated and measured $\Delta\lambda_H$ are weak (approximately 5% of the maximum possible horizontal
278 anisotropy $\Delta\lambda_H = 1$ (Fig. 4b), with the estimated one being slightly weaker than the measured
279 one). In contrast, both the estimated and measured vertical ice fabric anisotropy $\Delta\lambda_V$ increase
280 with depth (Fig. 4c). Similar to $\Delta\lambda_H$, the estimated $\Delta\lambda_V$ is also weaker than the measured $\Delta\lambda_V$.
281

282 Similarly to the ice core data, the radar-derived fabric shows a tendency to form clusters which increase in
283 strength with increasing depth (Fig. 4c). The differences seen in the eigenvalue magnitudes correspondingly
284 translate into the K and C classification: The estimated C values (colour of marks in Fig. 4c) are weaker
285 than the measured ones, particularly on the shallower part of the ice column. The minimum C value
286 estimated from radar at site p0 is 0.19, and the maximum is 1.81. In contrast, the ice core values are 0.36
287 and 2.35, respectively. The estimated $\Delta\lambda_H$ between 350 and 380 increases to 0.12 (Fig. 4b), resulting from
288 the corresponding change in λ_1 and λ_2 (Fig. 4a). This behaviour does not affect $\Delta\lambda_V$ (Fig. 4c), but it does
289 affect the K value (Fig. 4c) which is close to unity. However, no ice-core data are available at that depth to
290 validate this behaviour. It is important to note that Fig. 4c shows a limited range of fabric types, while Fig.
291 C1 in the appendix provides a fuller context for better comparison between measured and estimated fabric.
292 Although the fabric type is broadly captured, its depth variability is overestimated by the pRES data. This
293 overestimation stems from systematically low horizontal anisotropy values (blue line in Fig. 4b), which
294 are disproportionately amplified because the low horizontal anisotropy values appear in the denominator of K .
295

296 4.3. Spatial changes in ice-fabric and vertical strain rates along the 5 km transect

297 After comparing the consistency between the estimated eigenvalues derived from polarimetric radar data
298 at the p0 site and the measured ice core eigenvalues, we reconstruct ice-fabrics for all sites p1 to p14 along
299 the 5 km long transect. To interpret our results, we normalize distances and elevation with the ice thickness
300 at the dome ($H \simeq 550$ m). The distance of the pRES points from the dome denoted as X is normalized
301 as $x = X/H$. Additionally, elevation is expressed as the normalized ice height above the bed, denoted as

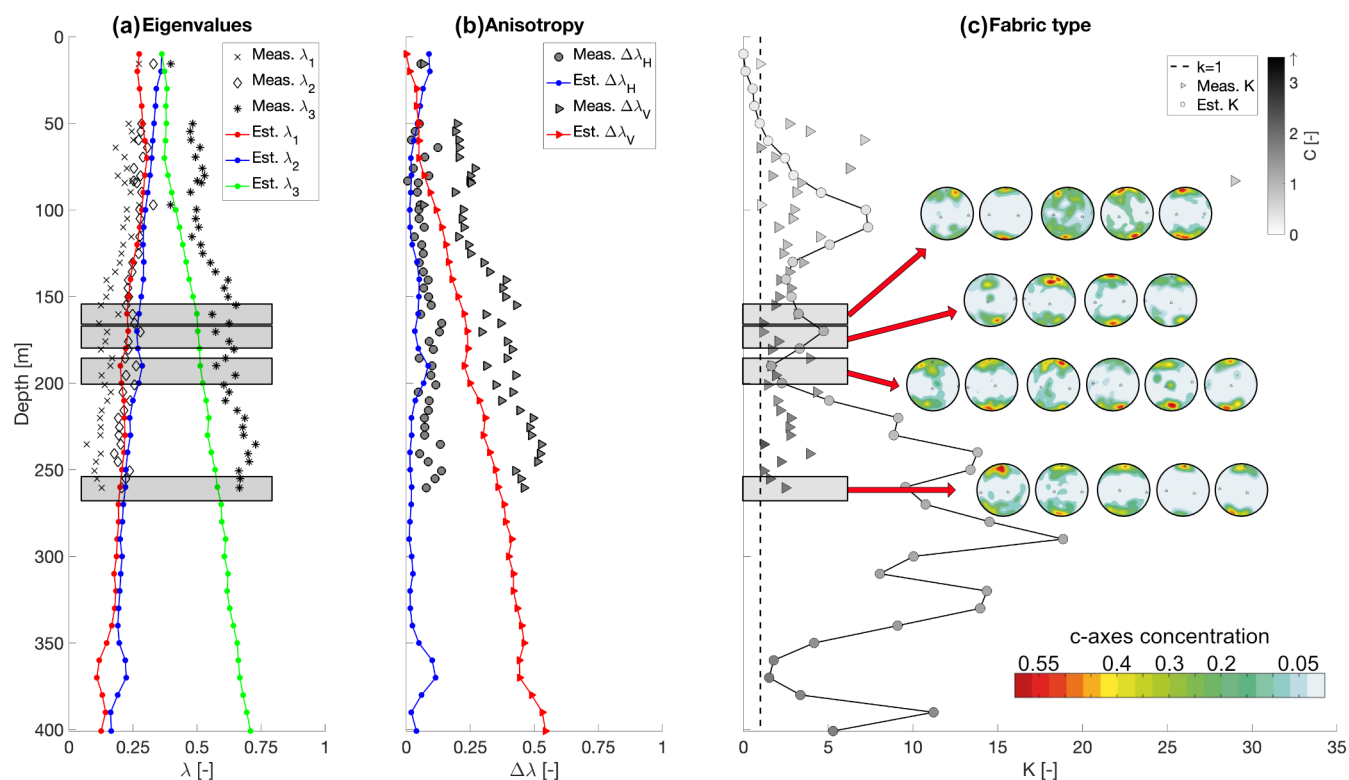


Figure 4: Comparison between estimated and measured (a) eigenvalues, (b) horizontal and vertical ice fabric anisotropy as $\Delta\lambda_H$ and $\Delta\lambda_V$, respectively and (c) Woodcock values K and C with density Schmidt diagrams measured from the ice core. Note that the estimated values are the results from the inverted radar data, and the measured values are from the ice-core laboratory analysis.

302 $z = (H - Z)/H$, where Z represents the depth. In this context, the mean bed elevation and mean surface
 303 elevation along the pRES profile are designated as $z = 0$ and $z = 1$, respectively. Subsequently, we employ
 304 linear interpolation to obtain the spatial variation of the fabric parameters along the 2D transect (Fig. B1).

305

306 Depth-averaged values of the horizontal anisotropy $\Delta\lambda_H$ show differences on both sides of the divide
 307 (Fig. B1a). On the south-eastern side, where ice is thicker, values of $\Delta\lambda_H$ are in general larger and more
 308 variable than on the north-western side. In the 30 – 35 % depth-interval, the averaged $\Delta\lambda_H$ exhibits a
 309 local maximum beneath the summit that is approximately one ice thickness wide and is asymmetrical. The
 310 north-western side also exhibits slightly smaller maxima beneath the ice-rise flanks. The spatial distribution
 311 of the magnitude of the strongest estimated eigenvector λ_3 (Fig. B1b) exhibits a similar pattern in terms of
 312 a local maximum beneath the divide and has generally larger values on the north-western side. The depth-
 313 average orientation of \vec{v}_2 , aligns within 10deg with the North-South direction (Fig. B1c). This direction

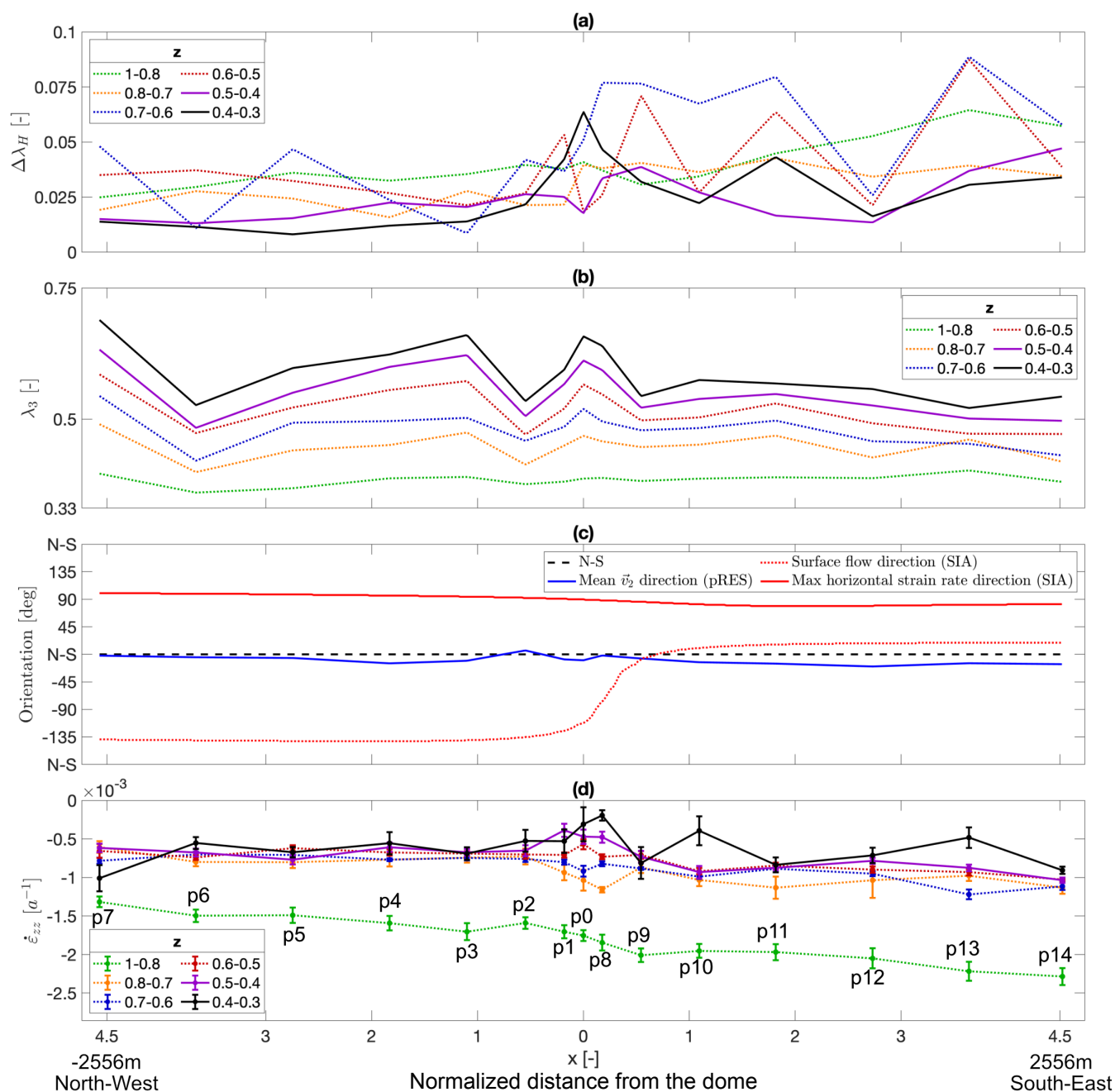


Figure 5: (a) Depth-averaged variation of $\Delta\lambda_H$ within a specific depth window. (b) Depth-averaged variation of λ_3 within a specific depth window. (c) Depth-averaged horizontal ice fabric orientation (blue line), surface flow direction derived from SIA (dashed red), and maximum strain direction derived from SIA (red line). (d) Vertical strain rates measured at each pRES site averaged over different depth intervals. Note that more negative strain rates indicate stronger deformation. The x-axis is the distance from the dome normalized by H .

314 is ~ 40 deg offset to the mean flow direction in the ice-rise flanks and ~ 81 deg offset to the direction of
315 maximum horizontal strain inferred from the SIA-based velocity field. The magnitude of the depth-averaged
316 vertical strain rates (Fig. B1d) is highest in the top 20 % of the ice thickness (80 to 100 % depth interval),
317 where the densification of firn is strongest. Vertical strain rates are also overall smaller in absolute value
318 in the thinner north-western flank than the thicker south-eastern flank. At approximately 50% of the ice
319 thickness, the vertical strain rates exhibit a pronounced (weakly double-peaked) minima beneath the divide
320 which extends laterally for 1-2 ice thickness into the ice-rise flanks.

321 4.4. Internal stratigraphy

322 The airborne UWB radar profiles (Fig. 6) image ice thickness and internal radar stratigraphy in profiles
323 located nearly perpendicular to the local ice divides (Fig. 1). The average ice thickness is between 500 and
324 600 m beneath the divides. The bed increases in elevation towards the west and deepens from the triple
325 junction into the landward direction. The bed beneath the saddle (Profile B-B') appears distinctly rougher
326 than beneath the dome area (Profile A-A'). The internal radar stratigraphy is clearly visible in both profiles
327 but cannot be identified unambiguously at depths deeper than the surface multiple (Koch and others,
328 2023a). Continuous tracking of the stratigraphy is also difficult in areas where internal layers are more
329 inclined (i.e., near the divides) (Holschuh and others, 2014), and in areas where the flight track is curved (Fig.
330 1). Nevertheless, internal radar stratigraphy close to the surface appear deeper in the south-eastern flanks
331 compared to the north-western flanks, and their syncline arching beneath the divide is clearly visible in B-B'
332 (i.e., beneath the saddle) and to a lesser extent also along A-A' (just north-west of the dome). The arches
333 increase in amplitude with increasing depth and are vertically aligned with today's divide position (Fig. 1).
334

335 5. DISCUSSION

336 Previous studies have investigated ice-rise evolution using flow-line modelling in combination with the
337 internal isochronal radar stratigraphy as principal observations (Drews and others, 2013, 2015; Goel and
338 others, 2017, 2018; Martín and others, 2009a,b; Martín and Gudmundsson, 2012; Hindmarsh and others,
339 2011). Two additional studies of a dome and ice rise, respectively, used the observed vertical strain rates
340 (Gillet-Chaulet and others, 2011; Kingslake and others, 2014). Here we use all of the previous observations
341 and add quad-polarimetric radar measurement as another possible observational constraint. We now
342 investigate whether those observations capture signatures of the Raymond effect and, if so, how these

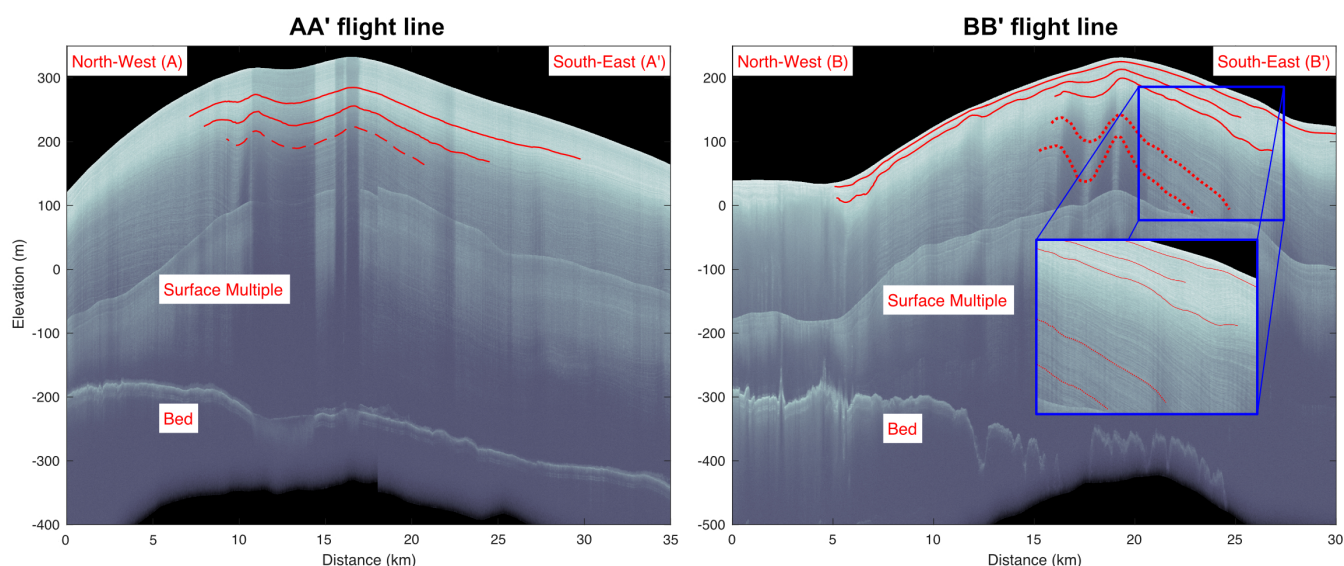


Figure 6: Airborne UWB radargrams crossing two ridges of the triple junction dome (A-A') and the saddle ridge (B-B'). Red curves highlight laterally coherent internal reflection horizons, and red dashed lines contain in parts data gaps, particularly in areas where the layers are more inclined.

343 can be contextualised with other geophysical observations of the contemporary flow regime. This may guide
 344 the application of a future 3D model (incl. thermo-mechanical coupling and anisotropic rheology) which is
 345 capable of simulating the complex dynamics occurring at triple junction ice rises. Given that the extraction
 346 of ice-fabric parameters from quad-polarimetric data using non-linear inversion has so far only once been
 347 compared with direct ice-core measurements (Ershadi and others, 2022), we first discuss the benefits and
 348 limitations of this method in general before moving on to investigate the flow history of HIR.

349 5.1. Applicability of the inferred the ice-fabric eigenvalues

350 The quad-polarimetric analysis has a limitation in that it assumes one of the principal eigenvectors
 351 points upwards. Although this assumption can be relaxed (Rathmann and others, 2022), it leads to a
 352 more complicated forward model for which the inversion is not yet established. However, (Rathmann and
 353 others, 2022) show that the polarimetric radar response of nadir-looking radars is comparatively insensitive
 354 to ice fabrics that are vertically tilted. However, beneath ice domes vertical compression is assumed to
 355 dominate, which is expected to lead to a vertical point maximum in the c -axes distribution (Budd and
 356 Jacka, 1989; Llorens and others, 2022) We, therefore, consider the assumption of horizontal and vertical
 357 eigenvectors to be justified, and not likely a cause for the systematic mismatch in magnitude that we

358 observe between the eigenvalues from the quad-polarimetric method and the ice-core-based values (Fig. 4a).

359

360 The systematic underestimation of $\Delta\lambda_H$ and $\Delta\lambda_V$ compared to ice-core values has to a lesser extent
361 also been observed at the ice-core site of the European Project for Ice Coring in Antarctica (EPICA) at
362 Concordia Dome C (EDC), however, it does not occur at the EPICA site in Dronning Maud Land (EDML)
363 (Ershadi and others, 2022). We investigated if using a scaling factor to the dielectric anisotropy for a single
364 crystal (commonly assumed to be 0.034 (Matsuoka and others, 1997)) can explain the underestimation.
365 However, the mismatch did not significantly improve when changing dielectric anisotropy within the reported
366 uncertainties. The inversion is also sensitive to the fabric orientation and backscatter ratio. The latter in
367 turn varies according to the ice-core data on shorter spatial scales than what the inversion can currently
368 resolve, particularly because it involves vertical averaging to smooth the phase gradient. The reason for the
369 underestimation of $\Delta\lambda_H$ and $\Delta\lambda_V$ therefore requires further investigation, but given that the gradients are
370 well reproduced, this does not hinder the interpretation of lateral ice-fabric variability.

371 5.2. pRES detects geo-referenced fabric orientation

372 The estimated \vec{v}_2 , as depicted in figure 5c, is derived solely from pRES data, without validation from field
373 datasets. To overcome this limitation, we used surface flow direction data obtained from SIA modeling to
374 compute the eigenvectors and eigenvalues of the strain rate tensor $\dot{\epsilon}$. When comparing \vec{v}_2 to the surface
375 flow direction, a deviation of $\sim 40^\circ$ is observed (Fig. 5c blue vs. dashed red). In contrast, when compared
376 to the direction of maximum horizontal strain rate, \vec{v}_2 shows a deviation of $\sim 81^\circ$ (Fig. 5c blue vs. solid red).

377

378 It is established by Alley (1992) that during ice deformation, c-axes consistently rotate towards
379 compressional axes and away from tensional axes. Also, the principles of fabric orientation under vertical
380 shortening is discussed by Passchier (1997) where the theory explains that basal planes rotate towards
381 the horizontal plane, which serves as the fabric attractor. Consequently, the perpendicular c-axes rotate
382 towards the vertical direction. The rotation is most rapid in the plane containing the direction of maximum
383 shortening (vertical) and maximum stretching. As a result, the variation in the horizontal c-axes, described
384 by λ_1 in the direction \vec{v}_1 , is narrowest in this plane. \vec{v}_2 is perpendicular to this direction in the horizontal
385 plane, hence it is expected to be oriented at 90° to the direction of maximum stretching, which indeed
386 corresponds to our observations in figure 5c ($\sim 81^\circ$). Also, as suggested by the pRES measurements, λ_1
387 and λ_2 exhibit similar intensities (weak $\Delta\lambda_H$), it follows that the same might hold true for $\dot{\epsilon}_1$ and $\dot{\epsilon}_2$.

388 Their combination would then yield maximum horizontal strain at approximately 45° from \vec{v}_1 and \vec{v}_2 . This
389 explains why \vec{v}_2 appears at approximately 45° from the flow direction in figure 5c ($\sim 40^\circ$).

390 **5.3. Synthesis of radar observations within the ice-dynamic setting of HIR**

391 The radar stratigraphy, the strain rates and the ice-fabric properties are all jointly influenced
392 by the ice-dynamic evolution of HIR and encode parts of its history, even though it is not
393 yet clear how rapidly ice-fabric parameters change with the ice-dynamic flow regime. Here
394 we synthesise the different datasets with a particular focus on the Raymond effect and
395 contextualise our findings with available modelling and observational studies of other ice rises.
396

397 The upward arches observed beneath the saddle (B-B', Fig. 6) are typical of ice rises in the sense that they
398 are located beneath today's divides and that they are asymmetrical in shape. For example, a syncline as
399 on the western side has also been observed at Derwael Ice Rise and explained with persistent accumulation
400 patterns including erosion of snow at the crest and re-deposition in the flanks (Drews and others, 2015).
401 Erosion of snow at the crest increases the amplitudes of the upward arches at larger depths which are,
402 however, primarily formed by the Raymond effect. Both mechanisms require a stable ridge divide position
403 and therefore testify that the saddle connecting HIR with the main ice sheet was stationary, probably for
404 several t_D , i.e., several thousands of years. Upward arching also occurs beneath the dome (at kilometre 10
405 in profile A-A', Fig. 6), but the amplitudes are smaller compared to the saddle. The eastern side of A-A' is
406 near-parallel to the eastern arm of the triple junction and hence strong upward arching is not expected in the
407 stratigraphy here. It is therefore unclear if the triple junction of HIR exhibits a Raymond cupola as modelling
408 would suggest (Hindmarsh and others, 2011), but if it does, the lower arch amplitudes could suggest that
409 the dome position is younger than the saddle, although three-dimensional effects may be responsible.
410

411 For a two-dimensional, plane strain flow regime, it is well understood that lateral differences in vertical
412 velocities that accompany the formation of Raymond arches, are expressed by corresponding patterns
413 in the vertical strain rates. More specifically, the vertical strain rates are expected to be smaller in
414 magnitude for 100 to 300 m depths (z from ~ 0.8 to 0.5) beneath the divide compared to the flanks
415 (Kingslake and others, 2014). Our observations (Fig. 5d) comply with these predictions, particularly for
416 330 to 380 m depths (z from ~ 0.4 to 0.3). At shallow depths (top 100 m) the vertical strain rates are
417 dominated by firn compaction, and deeper depth intervals could not be resolved. Observed magnitudes of

418 approximately 1.0×10^{-3} m/a are comparable to what has been observed at other triple junctions (i.e.,
419 Fletcher Promontory (Kingslake and others, 2014)), although the amplitude of the vertical strain rate
420 anomaly across the dome is smaller. Once a local divide or dome has formed, the effect on the velocity
421 field is instantaneous, and hence the vertical strain rates do not contain information about the ice-rise
422 history per se. However, ice-fabric types are strain-induced and develop over time (Budd and Jacka, 1989).
423 Consequently, if the dome position was temporally stable, corresponding signatures should appear in the
424 derived ice-fabric types from the quad-polarimetric analysis, indicating a temporarily stable dynamic regime.

425

426 Regarding the ice fabric, below 150 m where the distribution of the orientation of the fabric slowly
427 (low values on the density scale) evolves from a more random distribution in the top of the ice core
428 towards a single maximum closely centred on the vertical as expected from dominant uniaxial compression
429 at ice domes (e.g., Durand and others (2007)). The gradual strengthening of the fabric anisotropy is
430 clearly seen in the evolution of the measured eigenvalues (Fig. 4a). The small but increasing horizontal
431 anisotropy (Fig. 4b), indicating that the strain is not purely uniaxial flattening (compaction) but includes
432 differential deformation (such as lateral extension) in the horizontal plane which is coherent with the
433 complexity of the geomorphological setting (triple junction). The ice-fabric reconstruction from the
434 quad-polarimetric data shows that minima in the vertical strain rates (Fig. 5d) are accompanied by
435 corresponding maxima in $\Delta\lambda_H$ and λ_3 (Fig. 5a,b) in 330 to 380 m depth interval (z from ~ 0.4 to 0.3).
436 This is in line with measured ice fabric and two-dimensional model predictions of Martín and others
437 (2009a) which predicts a single maximum fabric which is stronger beneath the divide compared to the flanks.

438

439 A quantitative comparison in terms of timing between our observations and the model predictions of
440 Martín and others (2009a) is hampered in several ways: first, the assumed two-dimensional geometry
441 does not include the triple junction geometry of HIR, and second, the model predictions assume
442 an evolution from fully isotropic to fully anisotropic ice. The latter is unlikely to be the case for
443 HIR as demonstrated by the measured ice fabric data. Notwithstanding, in steady-state (i.e., at
444 approximately 10 times t_D) the predicted degree in ice-fabric anisotropy is larger than what is
445 reconstructed from quad-polarimetric data here. The reconstructed $\Delta\lambda_H$ consistently remains below
446 0.1 which is comparable to other domes such as Dome C, but is much weaker than what has been
447 observed in flank flow regimes such as the transient divide at the EDML drill site ($\Delta\lambda_H > 0.3$,

448 Ershadi and others (2022)). Based on these comparisons, it appears that HIR in terms of its ice-fabric
449 characteristic is not older than 4 times t_D (i.e., not older than approximately 5600 years). However, given
450 the discrepancies between the model assumptions and observations, this time interval is not well constrained.
451

452 Taken together, the UWB radar profile across the saddle suggests a temporally stable divide position.
453 The data at the dome are less conclusive in that sense, because arch amplitudes are smaller and because
454 the ice fabric is only weakly developed. One plausible scenario uniting this would be that HIR undergoes a
455 transition from a promontory towards an isle-type ice rise, which is a feature of deglaciation scenarios in this
456 particular region (Favier and Pattyn, 2015). Thinning in the saddle area would then result in comparatively
457 large arches relative to today's ice thickness in this area. The good match to the ice-core data reinforces
458 that quad-polarimetric surveys can be a reliable tool to further constrain ice-rise evolution, in particular
459 the influence of ice-anisotropy on Raymond arch evolution. For HIR, the comparatively weak ice -fabric
460 suggests a comparatively young dome. However, a single two-dimensional profile heavily simplifies the
461 dynamic complexity and modelling should account for these three-dimensional effects in the future.

462 6. CONCLUSION

463 We have investigated radar-derived properties of Hammarryggen Ice Rise (HIR): radar stratigraphy,
464 strain rates, and ice-fabrics. HIR is a representative triple junction promontory ice-rise,
465 making it an excellent laboratory to study ice dynamic processes, where we additionally,
466 had access to both the ice core for c-axes measurements and the corresponding radar data.
467

468 Upward arching in the stratigraphy indicates a stable ice divide in the saddle area over, at least,
469 several thousands of years. Upward arching beneath the dome is also observed but is less clear. Vertical
470 strain rates are dominated by firn compaction near the surface, and exhibit a minimum closer to the
471 bed indicative for the Raymond effect. The derived ice-fabric properties from quad-polarimetric radar
472 fit ice-core-based values. The horizontal anisotropy is weak and thus young compared to steady-state,
473 ice-dynamically evolved ice-fabric types predicted from two-dimensional models in comparable settings.
474 This is perhaps indicative of thinning of the saddle connecting the dome to the mainland. There are
475 also signatures of the Raymond effect in the ice-fabric. However, it is unclear how the triple junction
476 geometry of Hammarryggen Ice Rise impacts both the vertical strain rates and the ice-fabric development.
477 Previous studies have indicated that the region is ice-dynamically stable and comparatively resilient to

478 sea-level changes (Drews and others, 2015; Favier and Pattyn, 2015). Our study on Hammarryggen Ice
479 Rise provides further evidence for this stability, although it is the first instance where we suspect the
480 dome position may have a younger history compared to the connected saddle. This could be an important
481 consideration when using ice rises as proxies for ice-dynamic changes in their respective catchments.
482

483 Overall, the synthesis of the different radar observations has the potential to constrain unknown
484 parameters like the ice fabric in future ice-flow modelling, particularly if measurements cover larger
485 areas. We suggest that these additional geophysical constraints provide another step forward towards a
486 quantitative interpretation of Raymond arch amplitudes using observationally constrained, anisotropic,
487 three-dimensional ice-flow models of triple junctions, flow regimes common to many ice rises around
488 Antarctica.

489 **7. CODE AND DATA AVAILABILITY.**

490 The source code used in this study for pRES fabric analysis, strain rate analysis, and SIA
491 is available at [https://github.com/RezaErshadi/HammarryggenIceRiseSourceCode_FabricInversion_
492 Strainrates_SIA](https://github.com/RezaErshadi/HammarryggenIceRiseSourceCode_FabricInversion_Strainrates_SIA). The pRES and ice core data can be accessed at <https://zenodo.org/record/8095508>,
493 and the UWB data is available in Franke and others (2020), and Koch and others (2023b).

494 **8. AUTHOR CONTRIBUTIONS.**

495 MRE led the code development and writing of the manuscript. FP and SS collected the pRES data at HIR.
496 VT, JLT, SW led the ice core analysis. MRE, RD and CM designed the study outline. MRE analysed the
497 pRES data. RD, IK and OE led the UWB data analysis and interpretation. CH designed the SIA model.
498 FO inferred the vertical strain rate. PB and JLT led the interpretation of the fabric type. All authors
499 contributed to the writing of the final paper.

500 **9. COMPETING INTERESTS.**

501 At least one of the (co-)authors is an associate chief editor in JOG.

502 **10. ACKNOWLEDGEMENTS**

503 We would like to mention:

- 504 - M. Reza Ershadi and Reinhard Drews were supported by Deutsche Forschungsgemeinschaft (DFG)
505 Emmy Noether grant (grant no. DR 822/3-1).
- 506 - C. Henry was supported by DFG in the framework of the priority programme 1158 "Antarctic Research
507 with comparative investigations in Arctic ice areas" by a grant SCHA 2139/1-1.
- 508 - F. Oraschewsk was supported by a scholarship from the Studienstiftung des Deutschen Volkes.
- 509 - Sarah Wauthy benefited from a Research Fellow grant of the F.R.S.-F.N.R.S.
- 510 - Veronica Tsubluskaya benefited from a Research Fellow grant of the F.N.R.S.-FRIA.
- 511 - The ice core project was supported by The Belgian Research Action through Interdisciplinary Networks
512 (BRAIN-be) from the Belgian Science Policy Office (BELSPO) in the framework of the project "East
513 Antarctic surface mass balance in the Anthropocene: observations and multi-scale modelling (Mass2Ant)
514 with contract no. BR/165/A2/Mass2Ant.
- 515 - We gratefully acknowledge the data acquisition of the UWB radar data by Daniela Jansen and Steven
516 Franke and the contributions of Steven Franke to original data processing and the Ken Borek crew and
517 PES staff for logistic support.

518 11. FINANCIAL SUPPORT.

519 This research has been supported by

- 520 - Deutsche Forschungsgemeinschaft (DFG) Emmy Noether grant (grant no. DR 822/3-1).
- 521 - Deutsche Forschungsgemeinschaft (DFG) in the framework of the priority programme 1158 "Antarctic
522 Research with comparative investigations in Arctic ice areas" by a grant SCHA 2139/1-1.
- 523 - Studienstiftung des Deutschen Volkes.
- 524 - Research Fellow grant of the F.R.S.-F.N.R.S.
- 525 - Research Fellow grant of the F.N.R.S.-F.R.I.A.
- 526 - Belgian Research Action through Interdisciplinary Networks (BRAIN-be) from the Belgian
527 Science Policy Office (BELSPO) in the framework of the project "East Antarctic surface mass

528 balance in the Anthropocene: observations and multi-scale modelling (Mass2Ant) with contract no.
529 BR/165/A2/Mass2Ant.

530 References

- 531 Alfred-Wegener-Institut Helmholtz-Zentrum für Polar- und Meeresforschung (2016) Polar aircraft Polar5
532 and Polar6 operated by the Alfred Wegener Institute. *Journal of large-scale research facilities JLSRF*, **2**,
533 A87–A87 (doi: 10.17815/jlsrf-2-153)
- 534 Alley RB (1992) Flow-Law Hypotheses for Ice-Sheet Modeling. *Journal of Glaciology*, **38**(129), 245–256
535 (doi: 10.3189/S0022143000003658)
- 536 Bentley MJ, Ó Cofaigh C, Anderson JB, Conway H, Davies B, Graham AGC, Hillenbrand CD, Hodgson DA,
537 Jamieson SSR, Larter RD, Mackintosh A, Smith JA, Verleyen E, Ackert RP, Bart PJ, Berg S, Brunstein
538 D, Canals M, Colhoun EA, Crosta X, Dickens WA, Domack E, Dowdeswell JA, Dunbar R, Ehrmann
539 W, Evans J, Favier V, Fink D, Fogwill CJ, Glasser NF, Gohl K, Golledge NR, Goodwin I, Gore DB,
540 Greenwood SL, Hall BL, Hall K, Hedding DW, Hein AS, Hocking EP, Jakobsson M, Johnson JS, Jomelli
541 V, Jones RS, Klages JP, Kristoffersen Y, Kuhn G, Leventer A, Licht K, Lilly K, Lindow J, Livingstone SJ,
542 Massé G, McGlone MS, McKay RM, Melles M, Miura H, Mulvaney R, Nel W, Nitsche FO, O'Brien PE,
543 Post AL, Roberts SJ, Saunders KM, Selkirk PM, Simms AR, Spiegel C, Stollendorf TD, Sugden DE, van
544 der Putten N, van Ommen T, Verfaillie D, Vyverman W, Wagner B, White DA, Witus AE and Zwart
545 D (2014) A Community-Based Geological Reconstruction of Antarctic Ice Sheet Deglaciation since the
546 Last Glacial Maximum. *Quaternary Science Reviews*, **100**, 1–9 (doi: 10.1016/j.quascirev.2014.06.025)
- 547 Bons PD, Kleiner T, Llorens MG, Prior DJ, Sachau T, Weikusat I and Jansen D (2018) Greenland Ice Sheet:
548 Higher Nonlinearity of Ice Flow Significantly Reduces Estimated Basal Motion. *Geophysical Research*
549 *Letters*, **45**(13), 6542–6548 (doi: 10.1029/2018GL078356)
- 550 Brennan PV, Lok LB, Nicholls K and Corr H (2014) Phase-sensitive FMCW radar system for high-precision
551 Antarctic ice shelf profile monitoring. *IET Radar, Sonar & Navigation*, **8**(7), 776–786 (doi: 10/ghhvxh)
- 552 Budd WF and Jacka TH (1989) A Review of Ice Rheology for Ice Sheet Modelling. *Cold Regions Science*
553 *and Technology*, **16**(2), 107–144 (doi: 10.1016/0165-232X(89)90014-1)
- 554 Cavitte MGP, Goosse H, Wauthy S, Kausch T, Tison JL, Liefferinge BV, Pattyn F, Lenaerts JTM
555 and Claeys P (2022) From Ice Core to Ground-Penetrating Radar: Representativeness of SMB at
556 three ice rises along the Princess Ragnhild Coast, East Antarctica. *Journal of Glaciology*, 1–13 (doi:
557 10.1017/jog.2022.39)

- 558 Conway H and Wilbour C (1999) Evolution of snow slope stability during storms1. *Cold Regions Science*
559 *and Technology*, **30**(1), 67–77, ISSN 0165-232X (doi: [https://doi.org/10.1016/S0165-232X\(99\)00009-9](https://doi.org/10.1016/S0165-232X(99)00009-9))
- 560 CReSIS (2021) Cresis Toolbox [computer software] (doi: [10.5281/zenodo.5683959](https://doi.org/10.5281/zenodo.5683959)), retrieved from GitHub
- 561 Dall J (2010) Ice Sheet Anisotropy Measured with Polarimetric Ice Sounding Radar. In *2010 IEEE*
562 *International Geoscience and Remote Sensing Symposium*, 2507–2510 (doi: [10/dvwxpd](https://doi.org/10.1109/IGARSS.2010.5638959))
- 563 Davies BJ, Hambrey MJ, Smellie JL, Carrivick JL and Glasser NF (2012) Antarctic Peninsula Ice Sheet
564 evolution during the Cenozoic Era. *Quaternary Science Reviews*, **31**, 30–66 (doi: [10.1016/j.quascirev.](https://doi.org/10.1016/j.quascirev.2011.10.012)
565 [2011.10.012](https://doi.org/10.1016/j.quascirev.2011.10.012))
- 566 Drews R, Martín C, Steinhage D and Eisen O (2013) Characterizing the Glaciological Conditions at
567 Halvfarryggen ice dome, Dronning Maud Land, Antarctica. *Journal of Glaciology*, **59**(213), 9–20 (doi:
568 [10/ghvgvz](https://doi.org/10.1017/jhg.2013.10))
- 569 Drews R, Matsuoka K, Martín C, Callens D, Bergeot N and Pattyn F (2015) Evolution of Derwael Ice Rise
570 in Dronning Maud Land, Antarctica, over the last millennia. *Journal of Geophysical Research: Earth*
571 *Surface*, **120**(3), 564–579 (doi: [10/gm5w7w](https://doi.org/10.1002/jgrb.12577))
- 572 Durand G, Gillet-Chaulet F, Svensson A, Gagliardini O, Kipfstuhl S, Meyssonier J, Parrenin F, Duval P
573 and Dahl-Jensen D (2007) Change in Ice Rheology during Climate Variations – implications for ice flow
574 modelling and dating of the EPICA Dome C core. *Climate of the Past*, **3**(1), 155–167 (doi: [10/fskxzw](https://doi.org/10.1029/2006cl00327))
- 575 Ershadi MR, Drews R, Martín C, Eisen O, Ritz C, Corr H, Christmann J, Zeising O, Humbert A and
576 Mulvaney R (2022) Polarimetric Radar Reveals the Spatial Distribution of Ice Fabric at Domes and
577 Divides in East Antarctica. *The Cryosphere*, **16**(5), 1719–1739 (doi: [10.5194/tc-16-1719-2022](https://doi.org/10.5194/tc-16-1719-2022))
- 578 Ershadi MR, Drews R, Hawkins JD, Elliott J, Lines AP, Koch I and Eisen O (2024) Autonomous Rover
579 Enables Radar Profiling of Ice-Fabric Properties in Antarctica. *IEEE Transactions on Geoscience and*
580 *Remote Sensing*, **62**, 1–9 (doi: [10.1109/TGRS.2024.3394594](https://doi.org/10.1109/TGRS.2024.3394594))
- 581 Favier L and Pattyn F (2015) Antarctic Ice Rise Formation, Evolution, and Stability. *Geophysical Research*
582 *Letters*, **42**(11), 4456–4463 (doi: [10.1002/2015GL064195](https://doi.org/10.1002/2015GL064195))
- 583 Favier L, Gagliardini O, Durand G and Zwinger T (2012) A Three-Dimensional Full Stokes model of the
584 grounding line dynamics: Effect of a pinning point beneath the ice shelf. *The Cryosphere*, **6**(1), 101–112
585 (doi: [10.5194/tc-6-101-2012](https://doi.org/10.5194/tc-6-101-2012))
- 586 Favier L, Durand G, Cornford SL, Gudmundsson GH, Gagliardini O, Gillet-Chaulet F, Zwinger T, Payne
587 AJ and Le Brocq AM (2014) Retreat of Pine Island Glacier controlled by marine ice-sheet instability.

- 588 *Nature Climate Change*, **4**(2), 117–121 (doi: 10.1038/nclimate2094)
- 589 Franke S, Jansen D, Drews R and Eisen O (2020) Ice thickness from the coast of Dronning Maud
590 Land (Antarctica), recorded 2018/19 with the AWI UWB radar system (doi: 10.1594/PANGAEA.
591 911868), publication Title: Alfred Wegener Institute, Helmholtz Centre for Polar and Marine Research,
592 Bremerhaven
- 593 Franke S, Eisermann H, Jokat W, Eagles G, Asseng J, Miller H, Steinhage D, Helm V, Eisen O and Jansen
594 D (2021) Preserved landscapes underneath the Antarctic Ice Sheet reveal the geomorphological history of
595 Jutulstraumen Basin. *Earth Surface Processes and Landforms*, **46**(13), 2728–2745 (doi: 10.1002/esp.5203)
- 596 Franke S, Jansen D, Binder T, Paden JD, Dörr N, Gerber TA, Miller H, Dahl-Jensen D, Helm V, Steinhage
597 D, Weikusat I, Wilhelms F and Eisen O (2022) Airborne ultra-wideband radar sounding over the shear
598 margins and along flow lines at the onset region of the Northeast Greenland Ice Stream. *Earth System
599 Science Data*, **14**(2), 763–779 (doi: 10.5194/essd-14-763-2022)
- 600 Fromm T, Oberdieck C, Heitland T and Köhler P (2019) Expeditions to Antarctica: ANT-Land 2018/19
601 Neumayer Station III, Kohlen Station, Flight Operations and Field Campaigns (doi: 10.2312/BzPM\
602 _0733_2019)
- 603 Fujita S, Maeno H and Matsuoka K (2006) Radio-Wave Depolarization and Scattering within Ice Sheets:
604 A Matrix-Based Model to Link Radar and Ice-Core Measurements and Its Application. *Journal of
605 Glaciology*, **52**(178), 407–424 (doi: 10/dhz7vf)
- 606 Gillet-Chaulet F, Hindmarsh RCA, Corr HFJ, King EC and Jenkins A (2011) In-situ quantification of ice
607 rheology and direct measurement of the Raymond Effect at Summit, Greenland using a phase-sensitive
608 radar. *Geophysical Research Letters*, **38**(24) (doi: <https://doi.org/10.1029/2011GL049843>)
- 609 Goel V, Brown J and Matsuoka K (2017) Glaciological Settings and Recent Mass Balance of Blåskimen
610 Island in Dronning Maud Land, Antarctica. *The Cryosphere*, **11**(6), 2883–2896 (doi: 10.5194/
611 tc-11-2883-2017)
- 612 Goel V, Martín C and Matsuoka K (2018) Ice-Rise Stratigraphy Reveals Changes in Surface Mass
613 Balance over the Last Millennia in Dronning Maud Land. *Journal of Glaciology*, **64**(248), 932–942 (doi:
614 10.1017/jog.2018.81)
- 615 Goel V, Matsuoka K, Berger CD, Lee I, Dall J and Forsberg R (2020) Characteristics of Ice Rises and
616 Ice Rumples in Dronning Maud Land and Enderby Land, Antarctica. *Journal of Glaciology*, **66**(260),
617 1064–1078 (doi: 10.1017/jog.2020.77)

- 618 Greve R and Blatter H (2009) *Dynamics of Ice Sheets and Glaciers*. Advances in Geophysical and
619 Environmental Mechanics and Mathematics, Springer, ISBN 978-3-642-03414-5 978-3-642-03415-2 (doi:
620 10.1007/978-3-642-03415-2)
- 621 Hale R, Miller H, Gogineni S, Yan JB, Rodriguez-Morales F, Leuschen C, Paden J, Li J, Binder T,
622 Steinhage D, Gehrman M and Braaten D (2016) Multi-channel ultra-wideband radar sounder and
623 imager. In *2016 IEEE International Geoscience and Remote Sensing Symposium (IGARSS)*, 2112–2115
624 (doi: 10.1109/IGARSS.2016.7729545)
- 625 Hamilton GS and Whillans IM (2000) Point Measurements of Mass Balance of the Greenland Ice Sheet
626 using precision vertical Global Positioning System (GPS) surveys. *Journal of Geophysical Research: Solid*
627 *Earth*, **105**(B7), 16295–16301 (doi: 10.1029/2000JB900102)
- 628 Hargreaves ND (1977) The polarization of radio signals in the radio echo sounding of ice sheets. *Journal of*
629 *Physics D: Applied Physics*, **10**(9), 1285–1304 (doi: 10.1088/0022-3727/10/9/012)
- 630 Hargreaves ND (1978) The Radio-Frequency Birefringence of Polar Ice. *Journal of Glaciology*, **21**(85), 301–
631 313 (doi: 10/gjqntq)
- 632 Henry ACJ, Drews R, Schannwell C and Višnjević V (2022) Hysteretic Evolution of Ice Rises and Ice
633 Rumples in Response to Variations in Sea Level. *EGUsphere*, 1–25 (doi: 10.5194/egusphere-2022-128)
- 634 Hindmarsh RCA, King EC, Mulvaney R, Corr HFJ, Hiess G and Gillet-Chaulet F (2011) Flow at Ice-Divide
635 Triple Junctions: 2. Three-dimensional views of isochrone architecture from ice-penetrating radar surveys.
636 *Journal of Geophysical Research: Earth Surface*, **116**(F2) (doi: 10.1029/2009JF001622)
- 637 Holschuh N, Christianson K and Anandakrishnan S (2014) Power loss in dipping internal reflectors, imaged
638 using ice-penetrating radar. *Annals of Glaciology*, **55**(67), 49–56 (doi: 10.3189/2014AoG67A005)
- 639 Howat I, Porter C, Noh MJ, Husby E, Khuvis S, Danish E, Tomko K, Gardiner J, Negrete A, Yadav B,
640 Klassen J, Kelleher C, Cloutier M, Bakker J, Enos J, Arnold G, Bauer G and Morin P (2022) The
641 Reference Elevation Model of Antarctica - Strips, Version 4.1 (doi: 10.7910/DVN/X7NDNY)
- 642 Hutter K (1983) *Theoretical Glaciology*. Springer Netherlands (doi: 10.1007/978-94-015-1167-4)
- 643 Jordan TM, Schroeder DM, Castelletti D, Li J and Dall J (2019) A Polarimetric Coherence Method to
644 Determine Ice Crystal Orientation Fabric From Radar Sounding: Application to the NEEM Ice Core
645 Region. *IEEE Transactions on Geoscience and Remote Sensing*, **57**(11), 8641–8657 (doi: 10/gm5xnk)
- 646 Jordan TM, Schroeder DM, Elsworth CW and Siegfried MR (2020) Estimation of Ice Fabric within Whillans
647 Ice Stream using polarimetric phase-sensitive radar sounding. *Annals of Glaciology*, **61**(81), 74–83 (doi:

- 648 10/ghn49k)
- 649 Kingslake J, Hindmarsh RCA, Aðalgeirsdóttir G, Conway H, Corr HFJ, Gillet-Chaulet F, Martín C, King
650 EC, Mulvaney R and Pritchard HD (2014) Full-depth englacial vertical ice sheet velocities measured
651 using phase-sensitive radar. *Journal of Geophysical Research: Earth Surface*, **119**(12), 2604–2618 (doi:
652 <https://doi.org/10.1002/2014JF003275>)
- 653 Koch I, Drews R, Franke S, Jansen D, Oraschewski FM, Muhle LS, Višnjević V, Matsuoka K, Pattyn F
654 and Eisen O (2023a) Radar internal reflection horizons from multisystem data reflect ice dynamic and
655 surface accumulation history along the Princess Ragnhild Coast, Dronning Maud Land, East Antarctica.
656 *Journal of Glaciology*, 1–19 (doi: 10.1017/jog.2023.93)
- 657 Koch I, Drews R, Muhle LS, Franke S, Jansen D, Oraschewski F, Spiegel H, Višnjević V, Matsuoka K, Pattyn
658 F and Eisen O (2023b) Internal reflection horizons of ice shelves and ice rises in eastern Dronning Maud
659 Land (East Antarctica) from multisystem radio-echo sounding data (doi: 10.1594/PANGAEA.950383)
- 660 Langway CC (1958) Ice Fabrics and the Universal Stage. Technical report, U.S. Army Snow, Ice, and
661 Permafrost Research Establishment.
- 662 Lenaerts JTM, Brown J, Broeke MRVD, Matsuoka K, Drews R, Callens D, Philippe M, Gorodetskaya
663 IV, Meijgaard EV, Reijmer CH, Pattyn F and Lipzig NPMV (2014) High variability of climate and
664 surface mass balance induced by Antarctic ice rises. *Journal of Glaciology*, **60**(224), 1101–1110 (doi:
665 10.3189/2014JoG14J040)
- 666 Llorens MG, Griera A, Bons PD, Weikusat I, Prior DJ, Gomez-Rivas E, de Riese T, Jimenez-Munt
667 I, García-Castellanos D and Lebensohn RA (2022) Can changes in deformation regimes be inferred
668 from crystallographic preferred orientations in polar ice? *The Cryosphere*, **16**(5), 2009–2024 (doi:
669 10.5194/tc-16-2009-2022)
- 670 Martín C and Gudmundsson GH (2012) Effects of Nonlinear Rheology, Temperature and Anisotropy on the
671 Relationship between Age and Depth at Ice Divides. *The Cryosphere*, **6**(5), 1221–1229 (doi: 10/f4c9fm)
- 672 Martín C, Gudmundsson GH, Pritchard HD and Gagliardini O (2009a) On the Effects of Anisotropic
673 Rheology on Ice Flow, Internal Structure, and the Age-Depth Relationship at Ice Divides. *Journal of*
674 *Geophysical Research*, **114**(F4), F04001 (doi: 10/fhvht2)
- 675 Martín C, Hindmarsh RCA and Navarro FJ (2009b) On the Effects of Divide Migration, along-Ridge Flow,
676 and Basal Sliding on Isochrones near an Ice Divide. *Journal of Geophysical Research: Earth Surface*,
677 **114**(F2) (doi: 10/bgz2wj)

- 678 Martín C, Hindmarsh RCA and Navarro FJ (2006) Dating ice flow change near the flow divide at
679 Roosevelt Island, Antarctica, by using a thermomechanical model to predict radar stratigraphy. *Journal*
680 *of Geophysical Research: Earth Surface*, **111**(F1), 1–10 (doi: 10.1029/2005JF000326)
- 681 Matsuoka K, Hindmarsh RC, Moholdt G, Bentley MJ, Pritchard HD, Brown J, Conway H, Drews R, Durand
682 G, Goldberg D, Hattermann T, Kingslake J, Lenaerts JT, Martín C, Mulvaney R, Nicholls KW, Pattyn
683 F, Ross N, Scambos T and Whitehouse PL (2015) Antarctic Ice Rises and Rumples: Their properties and
684 significance for ice-sheet dynamics and evolution. *Earth-Science Reviews*, **150**, 724–745 (doi: 10/f7z95x)
- 685 Matsuoka T, Fujita S, Morishima S and Mae S (1997) Precise measurement of dielectric anisotropy in ice
686 Ih at 39 GHz. *Journal of Applied Physics*, **81**(5), 2344–2348 (doi: 10/c5zkfj)
- 687 Morlighem M (2022) Measures bedmachine Antarctica, Version 3 (doi: 10.5067/FPSU0V1MWUB6)
- 688 Morlighem M, Rignot E, Binder T, Blankenship D, Drews R, Eagles G, Eisen O, Ferraccioli F, Forsberg
689 R, Fretwell P, Goel V, Greenbaum JS, Gudmundsson H, Guo J, Helm V, Hofstede C, Howat I, Humbert
690 A, Jokat W, Karlsson NB, Lee WS, Matsuoka K, Millan R, Mougintot J, Paden J, Pattyn F, Roberts J,
691 Rosier S, Ruppel A, Seroussi H, Smith EC, Steinhage D, Sun B, van den Broeke MR, van Ommen TD,
692 van Wessem M and Young DA (2020) Deep Glacial Troughs and Stabilizing Ridges Unveiled beneath the
693 Margins of the Antarctic ice sheet. *Nature Geoscience*, **13**(2), 132–137 (doi: 10.1038/s41561-019-0510-8)
- 694 Nereson NA and Waddington ED (2002) Isochrones and Isotherms beneath Migrating Ice Divides. *Journal*
695 *of Glaciology*, **48**(160), 95–108 (doi: 10.3189/172756502781831647)
- 696 Nereson NA, Hindmarsh RCA and Raymond CF (1998) Sensitivity of the Divide Position at Siple
697 Dome, West Antarctica, to boundary forcing. *Annals of Glaciology*, **27**, 207–214 (doi: 10.3189/
698 1998AoG27-1-207-214)
- 699 Nicholls KW, Corr HF, Stewart CL, Lok LB, Brennan PV and Vaughan DG (2015) A ground-based radar
700 for measuring vertical strain rates and time-varying basal melt rates in ice sheets and shelves. *Journal of*
701 *Glaciology*, **61**(230), 1079–1087 (doi: 10/ghhvzt)
- 702 Passchier CW (1997) The Fabric Attractor. *Journal of Structural Geology*, **19**(1), 113–127 (doi: 10.1016/
703 S0191-8141(96)00077-6)
- 704 Pattyn F, Wauthy S, Sun S, Tison JL and Tsibulskaya V (2023) Polarimetric Radar Data and Ice Core
705 Data Collected at Hammarryggen Ice Rise, Antarctica (doi: 10.5281/zenodo.8095508)
- 706 Petit RJ, Aguinagalde I, de Beaulieu JL, Bittkau C, Brewer S, Cheddadi R, Ennos R, Fineschi S, Grivet
707 D, Lascoux M, Mohanty A, Müller-Starck G, Demesure-Musch B, Palmé A, Martín JP, Rendell S and

- 708 Vendramin GG (2003) Glacial Refugia: Hotspots but Not Melting Pots of Genetic Diversity. *Science*
709 (*New York, N.Y.*), **300**(5625), 1563–1565 (doi: <https://www.science.org/doi/10.1126/science.1083264>)
- 710 Philippe M, Tison JL, Fjøsne K, Hubbard B, Kjær HA, Lenaerts JTM, Drews R, Sheldon SG, De Bondt
711 K, Claeys P and Pattyn F (2016) Ice Core Evidence for a 20th Century Increase in Surface Mass
712 Balance in Coastal Dronning Maud Land, East Antarctica. *The Cryosphere*, **10**(5), 2501–2516 (doi:
713 10.5194/tc-10-2501-2016)
- 714 Rathmann NM, Lilien DA, Grinsted A, Gerber TA, Young TJ and Dahl-Jensen D (2022) On the Limitations
715 of Using Polarimetric Radar Sounding to Infer the Crystal Orientation Fabric of Ice Masses. *Geophysical*
716 *Research Letters*, **49**(1), e2021GL096244 (doi: 10/gpch5q)
- 717 Raymond CF (1983) Deformation in the Vicinity of Ice Divides. *Journal of Glaciology*, **29**(103), 357–373
718 (doi: 10/gjqnvn)
- 719 Rignot E, Mouginot J and Scheuchl B (2017) Measures insar-Based Antarctica Ice Velocity Map, Version
720 2 (doi: 10.5067/D7GK8F5J8M8R)
- 721 Rodriguez-Morales F, Gogineni S, Leuschen CJ, Paden JD, Li J, Lewis CC, Panzer B, Gomez-
722 Garcia Alvestegui D, Patel A, Byers, Crowe, Player, Hale, Arnold, Smith, Gifford, Braaten and Panton
723 (2014) Advanced Multifrequency Radar Instrumentation for Polar Research. *IEEE Transactions on*
724 *Geoscience and Remote Sensing*, **52**(5), 2824–2842 (doi: 10.1109/TGRS.2013.2266415)
- 725 Schannwell C, Drews R, Ehlers TA, Eisen O, Mayer C and Gillet-Chaulet F (2019) Kinematic Response of
726 Ice-Rise Divides to Changes in Ocean and Atmosphere Forcing. *The Cryosphere*, **13**(10), 2673–2691 (doi:
727 10/gm5xnt)
- 728 Schannwell C, Drews R, Ehlers TA, Eisen O, Mayer C, Malinen M, Smith EC and Eisermann H (2020)
729 Quantifying the Effect of Ocean Bed Properties on Ice Sheet Geometry over 40 000 Years with a Full-
730 Stokes model. *The Cryosphere*, **14**(11), 3917–3934 (doi: 10/ghm3hq)
- 731 Sun S, Hattermann T, Pattyn F, Nicholls KW, Drews R and Berger S (2019) Topographic Shelf Waves
732 Control Seasonal Melting Near Antarctic Ice Shelf Grounding Lines. *Geophysical Research Letters*, **46**(16),
733 9824–9832 (doi: 10.1029/2019GL083881)
- 734 Wauthy S, Tison JL, Inoue M, El Amri S, Sun S, Claeys P and Pattyn F (2023) Physico-Chemical Properties
735 of the Top 120 m of Two Ice Cores in Dronning Maud Land (East Antarctica): An open window on spatial
736 and temporal regional variability of environmental proxies. *Earth System Science Data Discussions*, 1–33
737 (doi: 10.5194/essd-2023-152)

- 738 Wesche C, Steinhage D and Nixdorf U (2016) Polar aircraft Polar5 and Polar6 operated by the Alfred
739 Wegener Institute. *Journal of large-scale research facilities JLSRF*, **2**, A87–A87 (doi: 10.17815/jlsrf-2-153)
- 740 Wilson CJL, Russell-Head DS and Sim HM (2003) The Application of an Automated Fabric Analyzer
741 System to the Textural Evolution of Folded Ice Layers in Shear Zones. *Annals of Glaciology*, **37**, 7–17
742 (doi: 10.3189/172756403781815401)
- 743 Woodcock NH (1977) Specification of Fabric Shapes Using an Eigenvalue Method. *Geological Society of
744 America Bulletin*, **88**(9), 1231 (doi: 10/fw4xp7)
- 745 Young TJ, Martín C, Christoffersen P, Schroeder DM, Tulaczyk SM and Dawson EJ (2020) Rapid
746 and Accurate Polarimetric Radar Measurements of Ice Crystal Fabric Orientation at the Western
747 Antarctic Ice Sheet (wais) Divide Deep Ice Core Site. Technical report, Ice sheets/Field Studies (doi:
748 10.5194/tc-2020-264)
- 749 Zeising O, Gerber TA, Eisen O, Ershadi MR, Stoll N, Weikusat I and Humbert A (2023) Improved
750 Estimation of the Bulk Ice Crystal Fabric Asymmetry from Polarimetric Phase Co-Registration. *The
751 Cryosphere*, **17**(3), 1097–1105 (doi: 10.5194/tc-17-1097-2023)

752 **Appendix A. LIMITATIONS IN DEPTH OF INVESTIGATION**

753 In Fig. A1, we present the ice thickness and coherence magnitude at the p0 radar site (located
754 at the centre of the profile). As detailed in Section 3.1, if the coherence magnitude falls
755 below 0.4 (red zone in Fig.A1), the signal is considered unreliable for further phase analysis.
756 As depicted in the figure, the coherence magnitude falls below 0.4 at approximately 400 m
757 depth. As a result, for all pRES data analysed in this study, only the top 400 m are used.

758

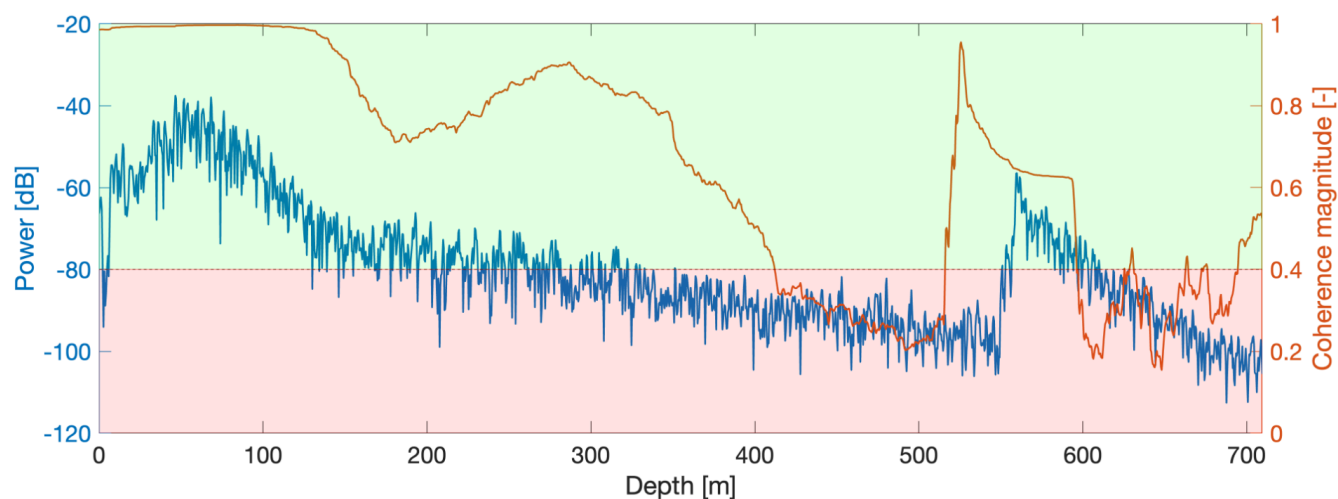


Figure A1: (a) Radar backscattered power (blue line) reveals the ice thickness. (b) The magnitude of complex polarimetric coherence between HH and VV signal (red line). The red zone is the area below 0.4 coherence magnitude.

759 **Appendix B. 2D INTERPOLATED FABRIC SPATIAL CHANGE**

760 A 2D interpolated spatial distribution of fabric properties inferred from pRES data is provided in figure B1.
 761 The values depicted in figure. B1a and B1b represent $\Delta\lambda_H$ and λ_3 , respectively, directly estimated from the
 762 pRES data. On the other hand, figure B1c and B1d illustrate the deviation between the estimated ice fabric
 763 orientation \vec{v}_2 and the surface flow direction from SIA and between \vec{v}_2 and the maximum strain direction
 764 from SIA, respectively.

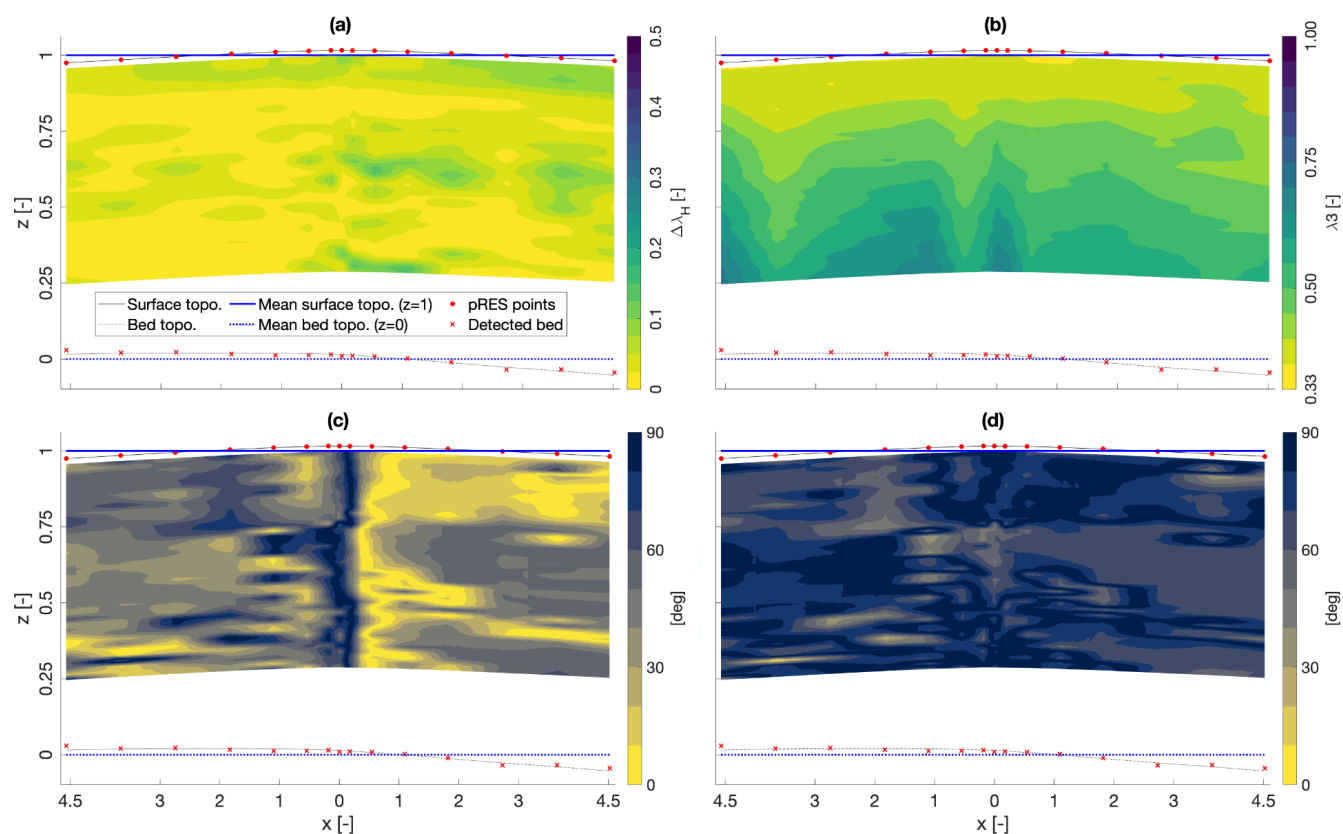


Figure B1: Showing the two dimensional interpolation of (a) horizontal ice fabric anisotropy. (b) Magnitude of the strongest eigenvalue (λ_3). (c) deviation of \vec{v}_2 from surface flow direction. (d) deviation of \vec{v}_2 from maximum strain rate direction. Note that both X and Y axes are normalised by the mean ice thickness ($H \simeq 550$ m).

765 **Appendix C. WOODCOCK PLOT (PRES AND ICE CORE)**

766 Woodcock (1977) introduced the parameter $K = \frac{\ln(\lambda_3/\lambda_2)}{\ln(\lambda_2/\lambda_1)}$ as a logarithmic ratio between the
767 Eigenvalues, dividing the ice fabric type into the cluster zone ($K > 1$) and the girdle zone
768 ($K < 1$). The extreme cases are the uniaxial girdle (K close to 0) and the uniaxial cluster (K
769 close to infinity), with $K = 1$ representing the transition zone. Additionally, Woodcock introduced
770 the parameter $C = \ln(\lambda_3/\lambda_1)$ as a measure of the preferred orientation strength. Higher C
771 values indicate a greater concentration of the c-axis and a lower noise level. By using Woodcock's
772 method, the ice fabric type obtained from estimated and measured Eigenvalues can be compared.

773

774 Here we regenerated the figure 1 from Woodcock (1977) add added some extra information to it. Hand-
775 drawn Schmidt diagrams illustrate the shape of the ice fabric type in each zone, where the top left and
776 bottom right show the uniaxial cluster and the uniaxial girdle, respectively. The isotropic ice fabric is
777 situated at the origin of the figure. Not that the thin sections in Schmidt diagrams from the ice core
778 analysis in Fig 4c are vertical while the Schmidt diagrams shown in Fig C1 are oblique. The estimated and
779 measured ice fabric types are depicted as green squares and black circles, respectively, within the 50 to 260
780 m range. Both the estimated and measured ice fabric types suggest that the fabric is in the weak cluster
781 zone, although the estimated fabric is slightly weaker compared to the measured fabric.

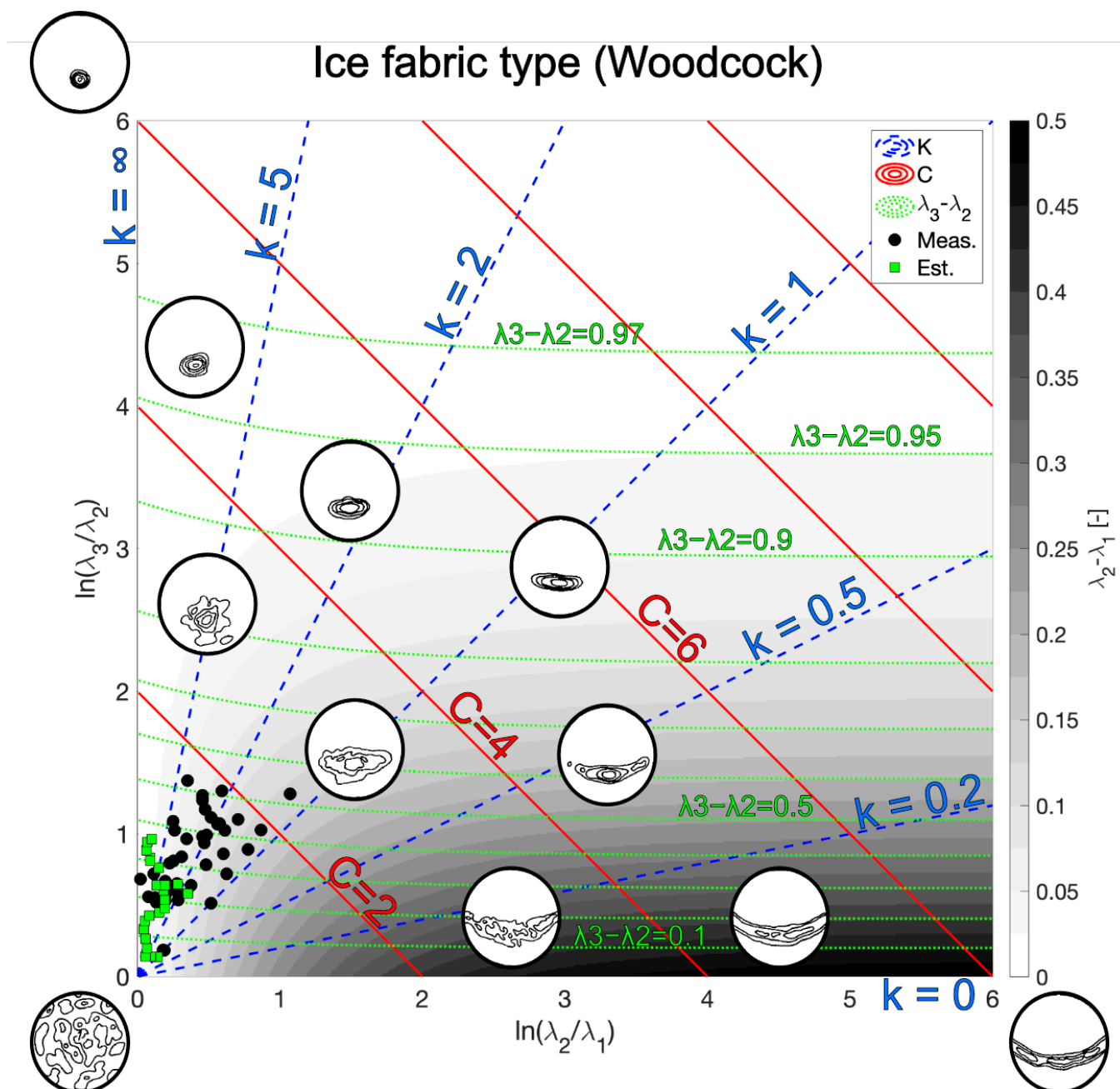


Figure C1: Regenerated Woodcock (1977), categorising the ice fabric type according to Woodcock's parameters. The background colour shows the change of $\Delta\lambda_H$, green dashed contours show the $\Delta\lambda_V$, blue dashed contours represent the K values, and red contours are the C values. The Schmidt diagrams are copied directly from Woodcock (1977). The green squares and black circles are estimated from radar data and measured from the ice core, respectively, between 50 to 260 m depth.

782 **Appendix D. SIA RESULTS**

783 The magnitude and orientation of surface velocity along with the magnitude and orientation of the maximum
784 horizontal strain estimated from SIA as explained in section 3.5 are shown all over HIR in Fig. D1

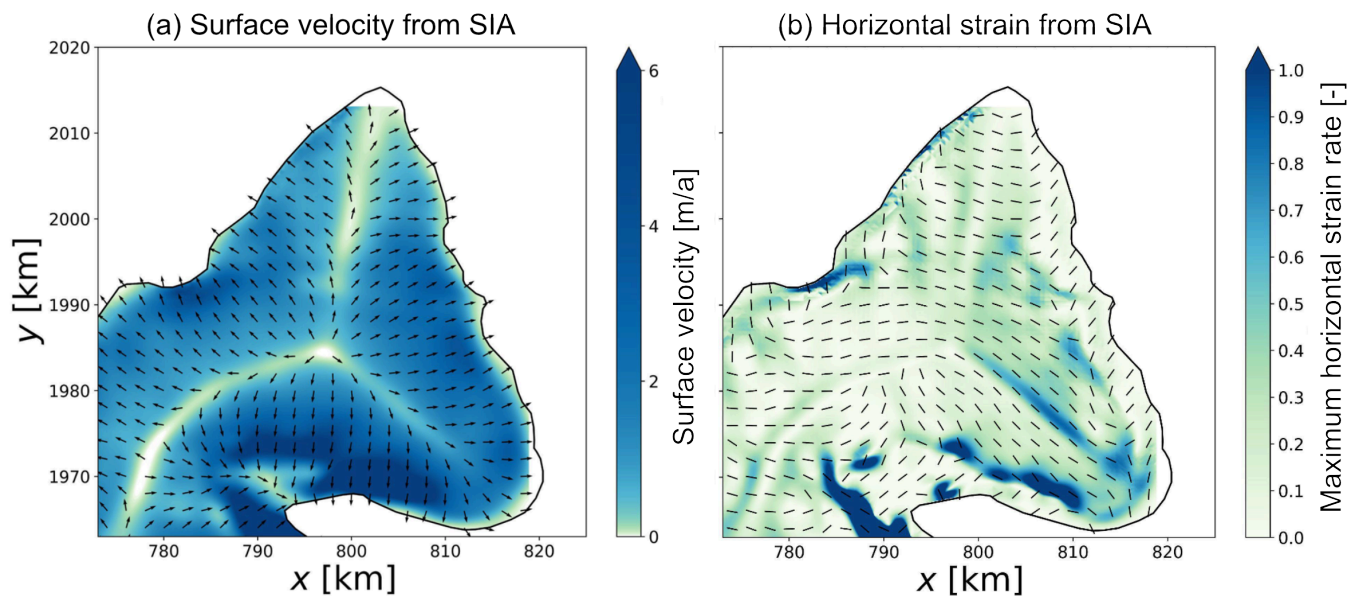


Figure D1: Estimated from SIA, (a) magnitude and direction of surface velocity. (b) magnitude and direction of maximum horizontal strain rate.